JETP Letters, Vol. 71, No. 3, 2000, pp. 102–105. Translated from Pis'ma v Zhurnal Éksperimental'noĭ i Teoreticheskoĭ Fiziki, Vol. 71, No. 3, 2000, pp. 152–156.

PLASMA, GASES

Liquid Plasma Crystal: Coulomb Crystallization of Cylindrical Macroscopic Grains in a Gas-Discharge Plasma

V. I. Molotkov*[1], A. P. Nefedov*, M. Yu. Pustyl'nik*, V. M. Torchinsky*, V. E. Fortov*, A. G. Khrapak*, and K. Yoshino**

** High Energy Density Research Center, Joint Institute for High Temperatures, Russian Academy of Sciences, Izhorskaya ul. 13/19, Moscow, 127412 Russia*

*** Faculty of Technology, Osaka University, Osaka, 565-0871 Japan*

Received December 28, 1999

Abstract—Ordered structures formed of 300-μm-long cylindrical nylon grains with diameters of 15 and 7.5 μm are obtained. In contrast to conventional spherical monodisperse grains, which, under certain conditions, form the plasma–dust Coulomb crystal, the cylindrical grains in the plasma acquire a charge of $\sim 7 \times 10^5$ electrons and form a structure similar to a liquid crystal. The parameter characterizing the nonideality of the dusty component of the plasma attains 10^6. Grains are suspended in the striation in the horizontal plane and line up in parallel with each other. © *2000 MAIK "Nauka/Interperiodica".*

PACS numbers: 52.25.Zb; 52.80.Hc

Macroscopic grains in a plasma acquire an electric charge. In the gas-discharge plasma, this is related to the higher electron mobility as compared to the ion mobility. The grains acquire the negative electrostatic potential that balances the fluxes of ions and electrons onto the grain surface. This so-called floating potential φ_{fl} of the grain is proportional to the electron temperature. The capacity C of the grain is proportional to its size. The electron energy in a low-pressure gas-discharge plasma is in the 1–10-eV range; therefore, 1–100-μm-size grains can acquire the charge $Z_p = e\varphi_{fl}C = (10^3–10^6)$ e. Since the potential energy of the Coulomb interaction is proportional to the product of the grain charges, the grain subsystem becomes nonideal much earlier than the gas-discharge plasma itself. Ikezi [1] was the first who drew attention to the possibility of the Coulomb crystallization of grains in a gas-discharge plasma. An interest in the study of a highly nonideal dusty plasma arose after plasma crystals were experimentally observed in RF [2–4] and dc [5–7] discharges. At present, nonideal dusty plasmas are being actively investigated in many laboratories. Plasma crystals of different structures (face-centered, space-centered, and hexagonal, as well as quasi-two-dimensional hexagonal in the vertical direction and chain in the vertical direction), were found. As the discharge parameters change, namely, the pressure decreases or the power increases, the point defects and dislocations emerge first; then, the crystal melts. The discussion of the results obtained to date is presented in reviews [8–10].

So far, in all the experimental studies of a nonideal dusty plasma, spherical grains were used; such a shape was also assumed in the theoretical investigations. However, it is well known that colloidal solutions, which have much in common with a dusty plasma, show much broader spectrum of the possible states in the case of strongly asymmetric needle-shaped or cylindrical grains [11, 12]. In this case, liquid phase and several liquid-crystal and crystal phases with different degrees of orientational and positional ordering were observed. In this paper, we present the results of the experimental study of the formation of ordered structures in a subsystem of 300-μm-long cylindrical nylon grains with a mass density of $\rho = 1.1$ g/cm^3 and diameters of $d = 15$ and 7.5 μm in the striations of a dc gas discharge.

The experiments were conducted with the device described in [13]. A glow discharge was excited in a cylindrical, vertically positioned glass tube with cold electrodes. The inner diameter of the tube was 3 cm, the length was 60 cm, and the interelectrode distance was 40 cm. The cylindrical grains were placed inside a container positioned at the upper end of the discharge tube. The container was shaken, and the grains fell into the discharge; some portion of them was trapped near the head of one of striations, where a strong electric field balanced out the gravity and the ion-entrainment forces. The observations were carried out with the use of a striplike, 150-μm-thick laser beam. The scattered laser radiation was recorded by a camera recorder. In experiments with lighter grains, the discharge tube was filled with pure neon. In order to suspend the heavier

[1] E-mail: molotkov@hedric.msk.su

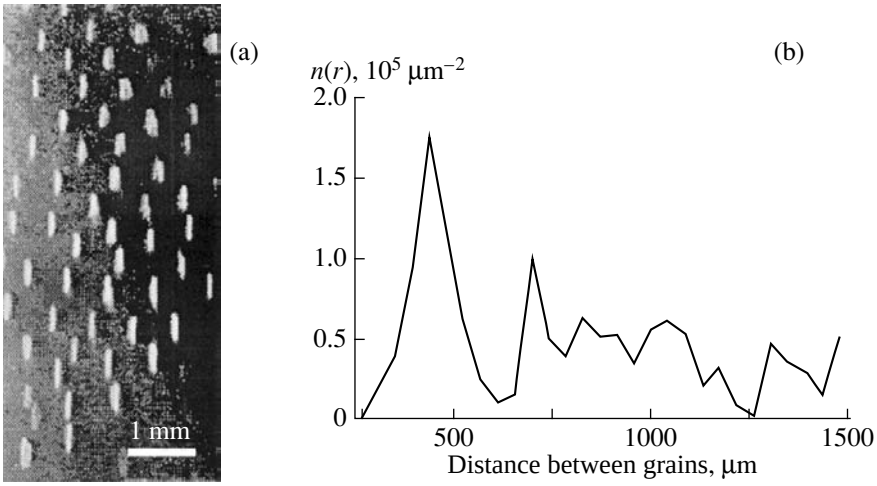

Fig. 1. (a) The image of the horizontal section of a structure formed of nylon grains 300 μm long and 15 μm in diameter and (b) the corresponding distribution function. The discharge is excited in a 1 : 1 neon–hydrogen mixture, the pressure is 0.9 torr, and the discharge current is 3.8 mA.

grains, we filled the tube with a neon–hydrogen mixture, which led to a decrease in the ratio of the length of the visible part of the striation to its total length and, consequently, to an increase in the electric field acting on grains.

Figure 1a presents a piece of the ordered structure formed of the heavier cylindrical grains (15 μm in diameter). Figure 1b shows the distribution function $n(r)$ representing the density of cylindrical grains at a distance r from the center of a given grain [13]. A short range order is clearly seen in the figure. All the particles lie in the plane perpendicular to the discharge axis and are oriented in a certain direction. It could be expected that levitating cylindrical grains should follow the cylindrical symmetry of the discharge. However, Fig. 1 shows no correlation between the grain orientation and the discharge symmetry. The preferential direction of the grain orientation also cannot be explained by the interaction between grains, because individual grains are oriented in the same direction as the grains in the structure (Fig. 2a). Moreover, there was no observed appreciable change in the grain orientation during the interaction between grains (Fig. 2b). Presumably, the preferential direction of the grain orientation is related to an insignificant asymmetry of the discharge tube. This is confirmed by the fact that the orientation can be changed by introducing an artificial perturbation into the discharge. The artificial perturbation was produced by a dielectric diaphragm with an aperture, which was located at a distance of several centimeters from the cathode. The formation of the positive column of the discharge began near the tube wall through a 1-cm-diameter aperture located at the diaphragm periphery. The distortion of the striation, which was visually observed, was evidence of the presence of an asymmetric component of the electric field. Rotation of the diaphragm (and, consequently, the aperture) by a certain angle resulted in change in the grain orientation in the same direction.

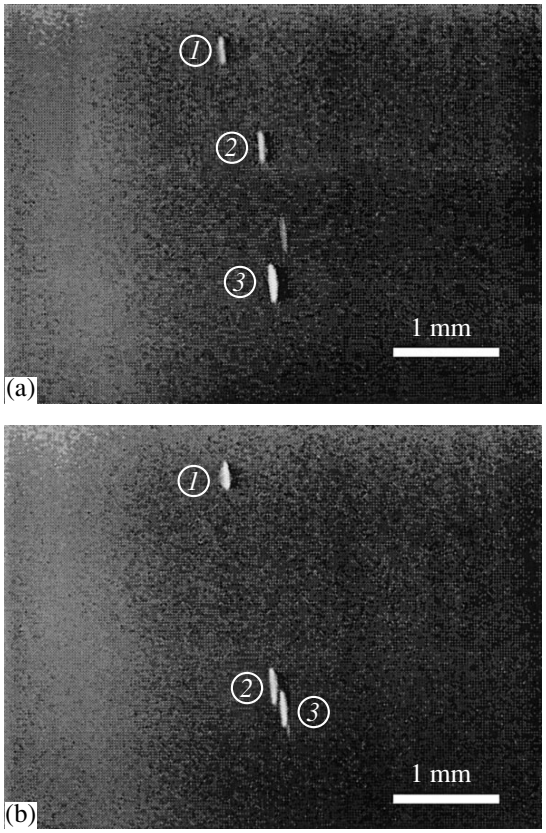

Fig. 2. Interaction of cylindrical nylon grains (300 μm long and 15 μm in diameter). The discharge is excited in a 1 : 1 neon–hydrogen mixture, the pressure is 1 torr, the discharge current is 4.4 mA, and the time interval between frames is 0.8 s.

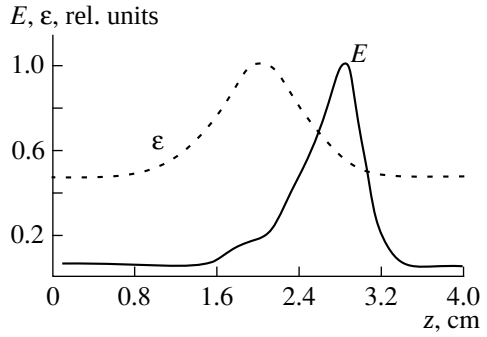

Fig. 3. The model distribution of the longitudinal electric field and average electron energy in a neon-discharge striation.

The levitation of the heavy cylindrical grains was observed only in the neon–hydrogen discharge. The presence of the molecular additive led not only to an increase in the electric field near the striation head, but also to a sharp decrease in the striation length. Therefore, the observed structures consisted of only few (four or five) layers.

The lighter grains of the same substance and with the same length but with a diameter of 7.5 μm were suspended even in the neon striations and formed the structures much more extended along the discharge axis. In this case, as in the case of the heavier grains, the structures also had a preferential direction.

At small pressures (~0.1 torr), in the lower parts of the structures, there were observed the oscillations with a wavelength of ~1 mm and a frequency of 20–50 Hz, similar to those observed in experiments with spherical grains [14].

Note that, for elongated cylindrical grains with $l/d \gg 1$, the charge-to-mass ratio is greater than for a spherical grain with the same mass. Thus, the grain shape used in this study is more advantageous from the viewpoint of grain levitation. Actually, the charge of a cylindrical grain with length l and radius a is

$$Z_p = eC\phi_{fl}, \tag{1}$$

where

$$C = l/2\ln(l/a). \tag{2}$$

For ϕ_{fl} = 30 V, l = 300 μm, and $2a$ = 15 μm, we have $Z_p = 7.7 \times 10^5$ e. Then, in order to balance the gravity acting on a nylon grain of the given size ($mg = 5.7 \times 10^{-10}$ N), the required electric field is $E \cong 30$ V/cm. Such an electric field is quite achievable in the striation head in a neon–hydrogen discharge. For a spherical grain, the required field is 1.3 times greater than for an elongated (l/d = 20) grain of the same mass; for l/d = 40, this difference increases to 1.7.

Let us consider the orientation stability of an elongated cylindrical grain in the striation. Figure 3 shows the model distributions of the electric field $E(z)$ and the average electron energy $\epsilon(z)$ in the striation that qualitatively agree with the experimental data [15]. Evidently, the levitation of dust grains can occur only in the region where the electric force acting on the grain increases toward the cathode. In the model distribution, this region approximately corresponds to the interval 1.2–2.8 cm. The moment of force acting on the cylindrical grain suspended in the striation is determined by

$$M(z_0, \alpha) = \int_{z_0 - \frac{l\cos\alpha}{2}}^{z_0 + \frac{l\cos\alpha}{2}} E(z)(z - z_0)\tan\alpha\frac{\lambda(z)dz}{\cos\alpha}, \tag{3}$$

where z_0 is the coordinate of the center of gravity of the grain; α is the angle the long axis of the grain makes with the direction of E; λ is the charge density determined by the local charging conditions,

$$\lambda(z) = \frac{\epsilon(z)}{2}\ln\left(\frac{m_i}{m_e}\frac{\epsilon(z)}{T_i}\right); \tag{4}$$

m_i and m_e are the ion and electron masses, respectively; and T_i is the ion temperature. One more factor influencing the grain orientation is the induced dipole moment of the cylindrical grain. However, estimates show that the moment of force produced by the interaction of this dipole moment with the longitudinal field of the discharge is small compared to M.

The angular dependence of the moment of force M in different points of the striation (l = 300 μm, T_i = 0.03 eV, maximum value of $E(z)$ is 30 V/cm, and the maximum value of $\epsilon(z)$ is 10 eV) is such that the stable grain position is horizontal. This is explained by a substantial variation of the charge density and the electric field of the discharge along the grain. The stable horizontal position is assisted by the electric-field gradient and the increase in the grain charge toward the cathode. Note that, for the distributions of the plasma parameters other than those considered above, the stable orientation can occur to be vertical.

The interaction energy of two grains positioned in parallel can be obtained by integrating the elementary interaction energy over the lengths of both grains. For the experimentally observed mutual position of two grains, this energy is about 10^5 eV. For the kinetic energy of grains equal to the gas temperature (0.03 eV), the interaction energy corresponds to a nonideality parameter of ~10^6.

Thus, the structures formed of the highly charged elongated cylindrical grains (with a length-to-diameter ratio of 20 or 40) exhibit the properties similar to those of nematic liquid-crystal structures [16]:

(i) the positions of the centers of gravity of the grains show the short range ordering,

(ii) the grains are oriented strictly in parallel with a certain common axis, and

(iii) the appearance of this axis is related to the violation of the cylindrical symmetry of the electric field.

ACKNOWLEDGMENTS

This work was supported by the Russian Foundation for Basic Research, project no. 99-02-18126.

REFERENCES

1. H. Ikezi, Phys. Fluids **29**, 1764 (1986).
2. J. H. Chu and L. I, Phys. Rev. Lett. **72**, 4009 (1994).
3. H. Thomas, G. E. Morfill, V. Demmel, *et al.*, Phys. Rev. Lett. **73**, 652 (1994).
4. Y. Hayashi and K. Tachibana, Jpn. J. Appl. Phys. **33**, L804 (1994).
5. V. E. Fortov, A. P. Nefedov, V. M. Torchinsky, *et al.*, Pis'ma Zh. Éksp. Teor. Fiz. **64**, 86 (1996) [JETP Lett. **64**, 92 (1996)].
6. V. E. Fortov, A. P. Nefedov, V. M. Torchinsky, *et al.*, Phys. Lett. A **229**, 317 (1997).
7. N. Sato, G. Uchida, R. Ozaki, *et al.*, in *Physics of Dusty Plasmas*, Ed. by M. Horany, S. Robertson, and B. Walch (AIP, New York, 1998), p. 239.
8. V. N. Tsytovich, Usp. Fiz. Nauk **167**, 57 (1997) [Phys. Usp. **40**, 53 (1997)].
9. V. E. Fortov, V. I. Molotkov, A. P. Nefedov, *et al.*, Phys. Plasmas **6**, 1759 (1999).
10. G. E. Morfill, H. M. Thomas, U. Konopka, *et al.*, Phys. Plasmas **6**, 1769 (1999).
11. H. Löwen, J. Chem. Phys. **100**, 6738 (1994).
12. H. Graf, *Freezing Transitions in Liquid Crystals* (Shaker, Aachen, 1998).
13. A. M. Lipaev, V. I. Molotkov, A. P. Nefedov, *et al.*, Zh. Éksp. Teor. Fiz. **112**, 2030 (1997) [JETP **85**, 1110 (1997)].
14. V. I. Molotkov, A. P. Nefedov, V. M. Torchinsky, *et al.*, Zh. Éksp. Teor. Fiz. **116**, 902 (1999) [JETP **89**, 477 (1997)].
15. Yu. B. Golubovskiĭ, S. U. Nisimov, and I. É. Suleĭmanov, Zh. Tekh. Fiz. **64**, 54 (1994) [Tech. Phys. **39**, 1005 (1994)].
16. P. G. de Gennes, *The Physics of Liquid Crystals* (Clarendon, Oxford, 1974; Mir, Moscow, 1977).

Translated by A. Smirnova

JETP Letters, Vol. 71, No. 3, 2000, pp. 106–110. Translated from Pis'ma v Zhurnal Éksperimental'noĭ i Teoreticheskoĭ Fiziki, Vol. 71, No. 3, 2000, pp. 157–163.

CONDENSED MATTER

Phase Separation in La–Pr Manganites and Its Evolution in a Magnetic Field

I. F. Voloshin[1, 6], A. V. Kalinov[1], S. E. Savel'ev[1], L. M. Fisher[1], N. A. Babushkina[2], L. M. Belova[2], D. I. Khomskiĭ[3, 4], and K. I. Kugel'[5]

[1] *State Research Center All-Russia Electrotechnical Institute, Moscow, 111250 Russia*

[2] *Russian Research Centre Kurchatov Institute, pl. Kurchatova 1, Moscow, 123182 Russia*

[3] *University of Groningen, 9747AG Groningen, The Netherlands*

[4] *Lebedev Institute of Physics, Russian Academy of Sciences, Leninskiĭ pr. 53, Moscow, 117924 Russia*

[5] *Institute of Theoretical and Applied Electrodynamics, Russian Academy of Sciences, Moscow, 127412 Russia*

Received November 18, 1999; in final form, December 29, 1999

Abstract—The effect of the magnetic field H on the electrical resistivity ρ and magnetic moment M of $(La_{0.25}Pr_{0.75})_{0.7}Ca_{0.3}MnO_3$ ceramic samples with various concentrations of ^{16}O and ^{18}O isotopes is studied. The behavior of $\rho(H)$ and $M(H)$ is characterized by an unusual shifted hysteresis loop and slow relaxation at some of its sections. The effects observed are interpreted within the framework of a model that takes into account the coexistence of regions of a ferromagnetic metal and an antiferromagnetic insulator and their evolution in an external magnetic field. © *2000 MAIK "Nauka/Interperiodica".*

PACS numbers: 72.60.+g; 75.30.Kz; 75.60.Ej

Manganites are characterized by a strong interaction of the electron, lattice, and spin subsystems, resulting in diversified phase transitions and various types of ordering. Metal–insulator and structural transitions are observed as well as various types of magnetic, orbital, and charge ordering. More and more theoretical [1–3] and experimental [4–6] works give evidence that inhomogeneous states and phase separation can exist in manganites. One of the most convenient objects for studying effects related to phase separation is a $(La_{1-y}Pr_y)_{1-x}Ca_xMnO_3$ system. When the relative content of La and Pr changes at a fixed Ca concentration, a transition between the ferromagnetic (FM) and charge-ordered (CO) phases occurs [7], near which this system may be unstable with respect to phase separation. Such a transition was discussed in detail in a number of recent papers [8–10]. In particular, it was revealed that, at $x = 0.3$, the transition between the FM and CO states can be caused even by the replacement of the ^{16}O isotope by ^{18}O [8] near the critical concentration of Pr ($y = 0.75$). By using neutron diffraction measurements, it was shown [10] that the composition with ^{16}O behaves as an antiferromagnetic at a temperature below $T_N = 150$ K, and, as the temperature decreases, the antiferromagnetic (AF) behavior changes to the ferromagnetic one at $T_C = 120$ K. At the same time, a sample with ^{18}O remains in the antiferromagnetic state down to the lowest temperatures. The features of the behavior exhibited by this system (slow relaxation, nonlinear volt-ampere characteristics [9], and coexistence of FM and AF reflections on neutron diffraction patterns [10]) show the possibility of the existence of phase separation in this concentration range. Recent studies of manganites by the scanning tunneling microscopy technique directly demonstrated the presence of inhomogeneous states in the vicinity of the insulator–metal transition [6].

This work is devoted to studies of magnetic and electric properties of a $(La_{0.25}Pr_{0.75})_{0.7}Ca_{0.3}MnO_3$ system containing either ^{16}O or ^{18}O. Unusual shifted hysteresis loops in the dependences of the magnetic moment and electrical resistivity on the magnetic field and a slow relaxation of M and ρ were observed in samples with both types of isotopes with qualitatively different magnetic properties. The presented results are interpreted within a framework of a kinetic model taking into account the coexistence of FM metal and AF dielectric domains as well as thermally activated transitions between these states.

Measurements were performed on rectangular $(La_{0.25}Pr_{0.75})_{0.7}Ca_{0.3}MnO_3$ ceramic samples with dimensions of $1 \times 1 \times 8$ mm and powders of the same composition. All the samples had either the natural oxygen isotope composition (mainly ^{16}O) or about 80 at. % of ^{18}O. A detailed preparation procedure and some characteristics of these samples are described in [8, 10].

The magnetic moment M was measured with a vibrating-coil magnetometer in fields H below 50 kOe.

[6] E-mail: voloshin@vei.ru

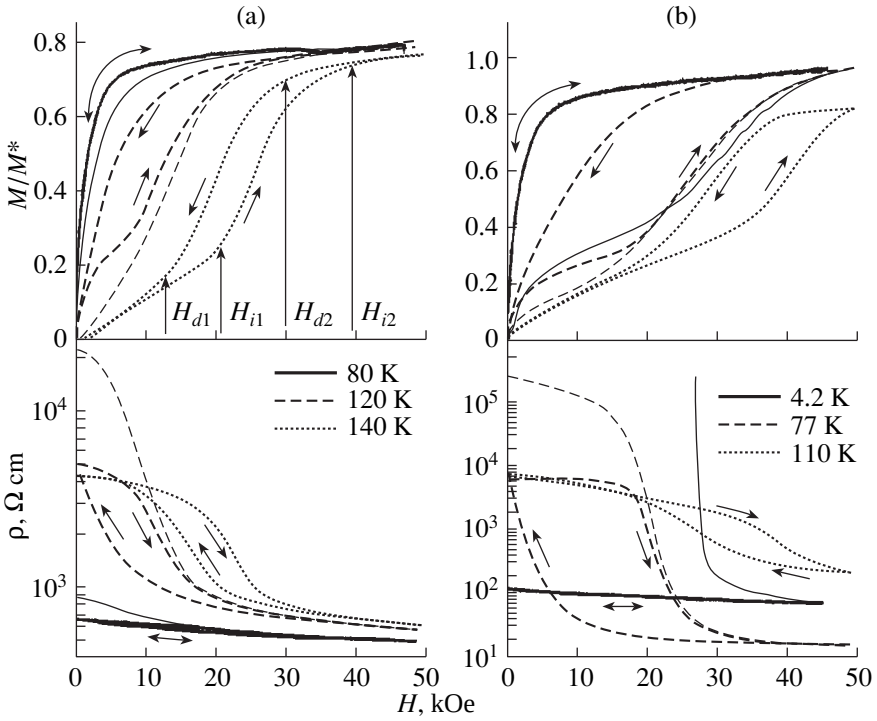

Fig. 1. Magnetization $M(H)/M^*$ and electrical resistivity $\rho(H)$ of ceramic samples with (a) ^{16}O and (b) ^{18}O. Thin lines correspond to the initial introduction of the magnetic field. The parameters M^*, H_i, and H_d are defined in the text.

In the case of sintered samples, their electrical resistivity ρ was simultaneously measured according to a four-probe scheme. The temperature (4.2–300 K) was monitored with a thermocouple attached to the sample. Isotherms $M(H)$ and $\rho(H)$ were measured after cooling the sample in the zero field. Typical curves for samples with ^{16}O and ^{18}O are shown in Figs. 1a and 1b. Here, the magnetic moment is given in relative units $M(H)/M^*$, where $M^* = M(H = 50$ kOe, $T = 4.2$ K); i.e., M^* is close to the saturation magnetic moment. Figures 1a and 1b presents two types of curves: the initial curves corresponding to the first field introduction and the curves establishing after the first half-cycle, which were preserved in subsequent cycles.

Three temperature ranges with different topographies of the $M(H)$ and $\rho(H)$ curves can be distinguished independently of the isotope composition of samples. At low temperatures ($T < T_1$), the hysteresis of steady-state curves is virtually absent, but they differ noticeably from the initial curve. This difference is appreciably larger in samples with ^{18}O and is especially pronounced in curves $\rho(H)$, where the change in the electrical resistivity reaches a value of several orders of magnitude being of percolation character. As the temperature rises ($T_1 < T < T_2$), the curves change qualitatively. A shifted hysteresis arises in the steady-state curves $\rho(H)$ and $M(H)$ at fields $H_{d1} < |H| < H_{i2}$. However, the difference between the initial curve and the steady-state one holds. As the temperature continues rising ($T > T_2$), the difference between the initial curve and the steady-state loop of the shifted hysteresis disappears, and the loop itself is shifted to higher fields. The differences in the temperature evolutions of the functions $M(H)$ and $\rho(H)$ for samples with different isotopic compositions are reduced to shifts of characteristic temperatures and magnetic fields at which certain features are manifested. In particular, for samples with ^{16}O, $T_1 \approx 80$ K and $T_2 \approx 120$ K, while for ^{18}O, $T_1 \approx 40$ K and $T_2 \approx 80$ K. All characteristic features of the magnetization behavior mentioned above are also manifested for powders. This also indicates that the effects investigated in this study are inherent properties of the substances under consideration and are not related to the structure of particular samples. A similar behavior of magnetization and electrical resistivity was observed in manganites [11, 12] and other systems [13].

In the mixed hysteresis region at $H_{i1} < H < H_{i2}$ and $H_{d1} < H < H_{d2}$, the magnetization and electrical resistivity underwent an appreciable relaxation, which had a logarithmic behavior at times of $\sim 10^2$ s. As an example, Fig. 2 shows a loop which was recorded at a sufficiently fast changes of an external magnetic field with stops at points *1*, *2*, *3*, and *4*. As we see, relaxation is virtually absent at points *1* and *3*, which do not fall within the field ranges mentioned above, and it is clearly pronounced at points *2* and *4* lying within ranges of $H_{i1} < H < H_{i2}$ and $H_{d1} < H < H_{d2}$, respectively.

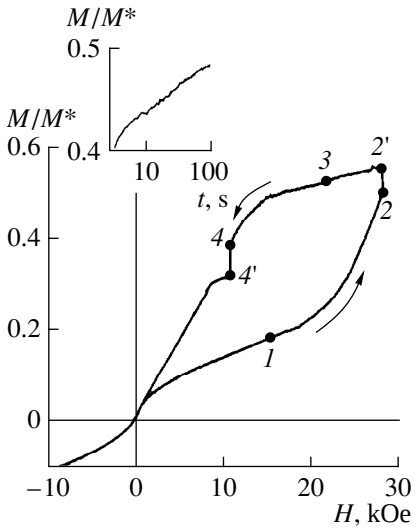

Fig. 2. Magnetization loop for the ^{18}O powder obtained at $dH/dt \approx 10$ kOe/min with 100-s-long pauses ($dH/dt = 0$) in characteristic regions marked with dots. In regions with smaller slopes of the shifted loop, e.g., at points *1* and *3*, $M(t) \approx$ const, while in regions with greater slopes, the relaxation represented by vertical segments (*2*, *2*') and (*4*, *4*') is observed. $T = 78$ K. The inset shows a time dependence of magnetization after an abrupt field jump from 0 to 28 kOe.

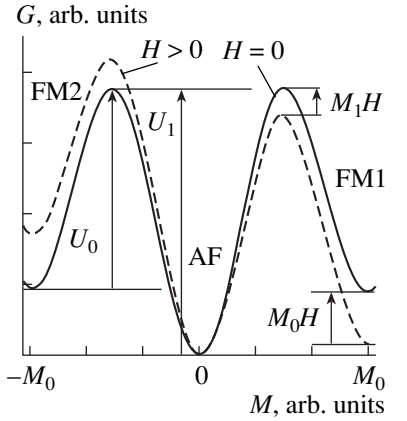

Fig. 3. Schematic dependence of the Gibbs potential G on magnetization M for $H = 0$ (solid line) and $H > 0$ (dashed line). The minima correspond to the antiferromagnetic (AF) and ferromagnetic (FM) states with different directions of the local magnetization (FM1, FM2).

The observed behavior of $M(H)$ and $\rho(H)$ can be naturally explained in the context of the coexistence of regions of metallic FM and dielectric AF phases. Such a pattern implies that the free energy of the system as a function of local magnetization has minima corresponding to AF and FM states (see Fig. 3). Changes in the concentrations of this or that phase is related to temperature-activated transitions. This approach was actively used for qualitative interpretation of the shifted hysteresis $\rho(H)$ and relaxation effects (e.g., [4, 12, 14]). However, these processes had no mathematical description for a long time. A system of kinetic equations was proposed in [15], which describes concentration variations of the FM phase with local magnetization M_0 oriented along the field ($C_{\uparrow\uparrow}$) and oppositely to it ($C_{\downarrow\downarrow}$), as well as of the AF phase ($C_{\uparrow\downarrow}$). This system of equations was successfully employed for description of static and relaxation dependences of the magnetization $M = M_0(C_{\uparrow\uparrow} - C_{\downarrow\downarrow}) = M_0\Delta C_F$ and the electrical resistivity that depends on the total concentration of the FM phase $C_F = C_{\uparrow\uparrow} + C_{\downarrow\downarrow}$. To describe the shifted hysteresis, it is basically important to take into account the dependence of the energy barriers $U_{\uparrow\downarrow}^{\uparrow\uparrow}$ and $U_{\uparrow\downarrow}^{\downarrow\downarrow}$, which determine the probabilities of the transitions from the AF to the corresponding FM states, on the field H (this dependence was not taken into consideration in [15]). Such an account leads to changes in the barrier heights. In fact, it can be presumed that, in the first approximation, the depth of the AF free-energy minimum remains unaltered (Fig. 3), while the depth of the FM minimum with the moment parallel to **H** changes by $\mathbf{M_0H}$. In addition, the height of the barrier separating these states decreases by a certain value $\mathbf{M_1H}$ ($M_1 < M_0$). Thus, the barrier height decreases for the AF-to-FM transition and increases for the reverse transition. As a result, for these barriers, we have $U_{\uparrow\uparrow}^{\uparrow\downarrow} = U_0 + (M_0 - M_1)H$, $U_{\uparrow\downarrow}^{\uparrow\uparrow} = U_1 - (M_0 - M_1)H$, $U_{\downarrow\downarrow}^{\uparrow\downarrow} = U_0 - (M_0 - M_1)H$, $U_{\uparrow\downarrow}^{\downarrow\downarrow} = U_1 + (M_0 - M_1)H$, where U_0 and U_1 are the corresponding barriers at $H = 0$. The following system of equations can be written for transitions between different states:

$$\frac{\partial C_{\uparrow\uparrow}}{\partial \tau} = -\exp\left(-\frac{U_{\uparrow\uparrow}^{\uparrow\downarrow}}{T}\right)C_{\uparrow\uparrow} - \exp\left(-\frac{U_{\uparrow\uparrow}^{\downarrow\downarrow}}{T}\right)C_{\uparrow\uparrow} + \exp\left(-\frac{U_{\uparrow\downarrow}^{\uparrow\uparrow}}{T}\right)C_{\uparrow\downarrow} + \exp\left(-\frac{U_{\downarrow\downarrow}^{\uparrow\uparrow}}{T}\right)C_{\downarrow\downarrow},$$

where τ is the dimensionless time. The second equation results from the replacement of the indices $\uparrow\uparrow$ with $\downarrow\downarrow$ and vice versa. The concentration of the AF phase can be found from the normalization condition $C_{\uparrow\uparrow} + C_{\downarrow\downarrow} + C_{\uparrow\downarrow} = 1$.

The linear system of equations derived allows us to calculate the intrinsic times $\tau_1(H, T)$ and $\tau_2(H, T)$ and to determine the stationary solutions C_F^{st}, $\Delta C_F^{st} = \tanh(M_0H/T)C_F^{st}$. At a reasonable selection of parameters of the problem, τ_1, related to remagnetization of ferromagnetic regions, turns out to be much smaller than τ_2 (see also [15]). The time τ_2, which determines the relaxation rate under changes of the AF phase concentration, is given by the formula

$$\tau_2^{-1}(H) = 2\exp(-U_1/T)\cosh(M_1H/T) + \exp(-U_0/T)\frac{\cosh(M_1H/T)}{\cosh(M_0H/T)}. \quad (1)$$

The first term in (1) associated with AF ⟶ FM1, FM2 transitions increases monotonically with H, and the second term related to reverse transitions diminishes with increasing H. As a result, the function $\tau_2(H)$ is nonmonotonic. An appreciable relaxation is observed, when τ_2 is of the order of magnitude of the characteristic measurement time τ^*. As a consequence of a nonmonotonic behavior of $\tau_2(H)$, a field interval $H_d < H < H_i$ may exist, within which $\tau^*/\tau_2 < 1$ and the FM phase concentration is frozen (see the solid curve in Fig. 4). Outside of this interval, the system is fast enough to follow changes in the external field and to maintain the equilibrium values C_F^{st} and ΔC_F^{st}. Thus, when the field value exceeds H_i, the system is defrosted and the concentration rapidly changes from $C_F^{st}(H_d)$ to $C_F^{st}(H_i)$. When the magnetic field begins decreasing, the FM phase is frozen at the point $H = H_i$ with $C_F^{st}(H_i)$ and the system holds this concentration until $H = H_d$ is reached, where C_F changes jumpwise up to $C_F^{st}(H_d)$. Such an evolution pattern of the magnetic phases accounts for the hysteresis of $\rho(C_F(H))$ and $M(H)$. In order to account for the differences between the initial curves and steady-state ones and for the disappearance of the shifted hysteresis at low temperatures, it is sufficient to study the temperature dependence of τ^*/τ_2. It can be shown that, when the temperature falls below a certain threshold value T_f, the parameter τ^*/τ_2 is determined by a function resembling that shown with the dashed line in Fig. 4. At $T < T_f$, the system becomes frozen even at $H = 0$ with a certain concentration $C_F(0)$ formed during cooling in the zero field. As the magnetic field increases to $H = H_i$, the FM phase concentration changes from $C_F(0)$ to $C_F^{st}(H_i)$. At further cyclic changes in the external field in a range $-H_i < H < H_i$, the FM phase concentration always remains stable $C_F(H_i) \neq C_F(0)$; i.e., the initial curve is never reproduced, and the hysteresis disappears.

In order to describe the logarithmic relaxation and the shape of the hysteresis loops observed, it is necessary to take into consideration the possible spread in barriers (e.g., as it was done in [15]). This leads to spreads in the field values: $H_{i1} < H < H_{i2}$ and $H_{d1} < H < H_{d2}$. It was assumed that the barrier heights U_0 and U_1 are distributed uniformly within certain fixed intervals. Their bounds were chosen so that the AF ground state was harnessed at $T = 0$. Figure 5 shows the calculated dependences $C_F(H)$ and $M(H)$, accounting for the barrier height spreads. Within the framework of this model, it is also possible to qualitatively explain relaxation effects observed experimentally. It is obvious that an appreciable phase-concentration relaxation and the corresponding relaxation of M and ρ must occur at $\tau^*/\tau_2 \approx 1$, i.e., at fields $H_{i1} < H < H_{i2}$ and $H_{d1} < H < H_{d2}$.

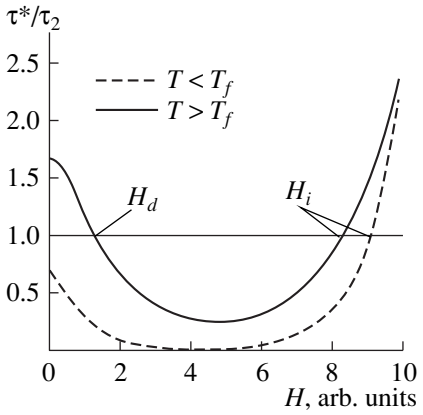

Fig. 4. Ratio τ^*/τ_2 versus magnetic field for two temperatures.

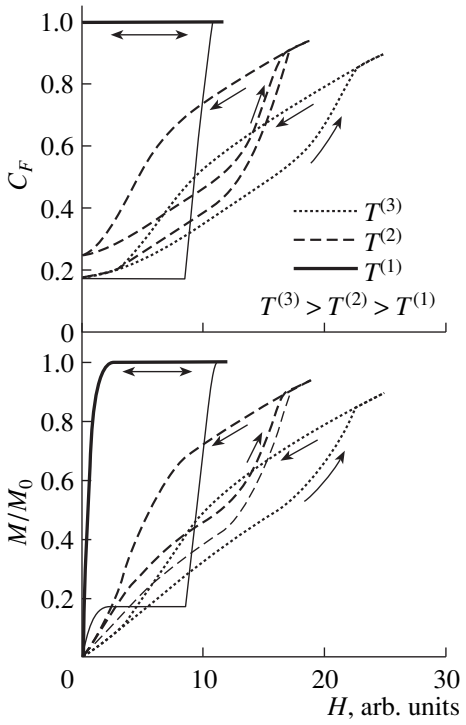

Fig. 5. Calculated dependences of the total FM-phase concentration C_F and magnetization M on the magnetic field for the set of parameters corresponding to various magnetization regimes (see Fig. 1). Thin lines correspond to the initial introduction of the field (similar to Fig. 1).

In conclusion, it should be noted that the anomalies of static and relaxation characteristics in mixed La–Pr manganites can be understood by using a simple phenomenological model that takes into account the phase separation in this system. Presumably, the model developed may be useful in predicting and interpreting new effects in materials with very large magnetoresistance.

ACKNOWLEDGMENTS

This work was supported by INTAS, grants nos. 97-0963 and 97-11954; Russian–Dutch Research Cooperation Program; Basic Research Foundation of Netherlands (FOM), and OXSEN European Program.

We are grateful to V.A. Yampol'skiĭ for useful discussions.

REFERENCES

1. É. L. Nagaev, Usp. Fiz. Nauk **166**, 833 (1996) [Phys. Usp. **39**, 781 (1996)].
2. A. Moreo, S. Yunoki, and E. Dagotto, Science **283**, 2034 (1999).
3. M. Yu. Kagan, D. I. Khomskiĭ, and M. V. Mostovoy, Eur. Phys. J. B **12**, 217 (1999).
4. H. Kuwahara, Y. Tomioka, A. Asamitsu, *et al.*, Science **270**, 961 (1995).
5. M. Uehara, S. Mori, C. H. Chen, and S.-W. Cheong, Nature **399**, 560 (1999).
6. M. Fäth, S. Freisem, A. A. Menovsky, *et al.*, Science **285**, 1540 (1999).
7. H. Y. Hwang, S.-W. Cheong, P. G. Radaelli, *et al.*, Phys. Rev. Lett. **75**, 914 (1995).
8. N. A. Babushkina, L. M. Belova, O. Yu. Gorbenko, *et al.*, Nature **391**, 159 (1998); J. Appl. Phys. **83**, 7369 (1998).
9. N. A. Babushkina, L. M. Belova, D. I. Khomskiĭ, *et al.*, Phys. Rev. B **59**, 6994 (1999).
10. A. M. Balagurov, V. Yu. Pomjakushin, D. E. Sheptyakov, *et al.*, Phys. Rev. B **60**, 383 (1999).
11. H. Kuwahara, Y. Moritomo, Y. Tomioka, *et al.*, Phys. Rev. B **56**, 9386 (1997).
12. M. Tokunaga, N. Miura, Y. Tomioka, and Y. Tokura, Phys. Rev. B **60**, 6219 (1999).
13. I. Chiorescu, W. Wernsdorfer, A. Müller, *et al.*, cond-mat/9911180.
14. A. Anane, J.-P. Renard, L. Reversat, *et al.*, Phys. Rev. B **59**, 77 (1999).
15. L. M. Fisher, A. V. Kalinov, S. E. Savel'ev, *et al.*, J. Phys.: Condens. Matter **10**, 9769 (1998).

Translated by A. Seferov

JETP Letters, Vol. 71, No. 3, 2000, pp. 111–113. From Pis'ma v Zhurnal Éksperimental'noĭ i Teoreticheskoĭ Fiziki, Vol. 71, No. 3, 2000, pp. 164–168.

CONDENSED MATTER

Nonohmic Coulomb Drag in the Ballistic Electron Transport Regime[1]

V. L. Gurevich and M. I. Muradov

Solid State Physics Department, Ioffe Physicotechnical Institute, Russian Academy of Sciences, St. Petersburg, 194021 Russia

Received December 16, 1999

Abstract—We developed the theory of Coulomb drag current induced in a one-dimensional nanowire by the ballistic nonohmic current in a nearby parallel nanowire under the ballistic transport regime. As in the ohmic case, we predict sharp oscillations of the drag current as a function of gate voltage or chemical potential of electrons. We also study the dependence of drag current on the voltage V across the driving wire. For relatively large values of V, the drag current is proportional to V^2. © *2000 MAIK "Nauka/Interperiodica".*

PACS numbers: 73.20.Dx; 73.61.-r

The purpose of this paper is to study the Coulomb drag current for the ballistic (collisionless) electron transport in a nanowire under the action of a ballistic driving nonohmic current in an adjacent parallel nanowire. The possibility of the Coulomb drag effect in the ballistic regime in quantum wires has been demonstrated by Gurevich, Pevzner, and Fenton [1][2] and was experimentally observed by Debray *et al.* in [2]. If two wires, 1 and 2, are near one another and parallel, the drag force due to the ballistic current in wire 2 acts as a kind of constant acceleration on the electrons of wire 1 via the Coulomb interaction.

We assume that the largest dimension of the structure is smaller than the electron mean free path (typically a few μm). The nanoscale systems of this type are characterized by low electron densities, which may be varied by means of the gate voltage.

Following [1], we assume that the drag current in wire 1 is much smaller than the driving ballistic current in wire 2 and calculate the drag current by iterating the Boltzmann equation for wire 1. We have

$$v\frac{\partial F^{(1)}}{\partial z} = -I^{(12)}\{F^{(1)}, F^{(2)}\}, \tag{1}$$

where $F^{(1,2)}$ are the electron distribution functions in wires 1 and 2, respectively; $v = p/m$ is the electron velocity; p is the x-component of electron quasimomentum; and the x-axis is parallel to the wires. The collision integral takes into account only the interwire electron–electron scattering; otherwise, the electron motion in both wires is considered as ballistic. Now,

$$I^{(12)}\{F^{(1)}, F^{(2)}\} = \sum_{n'p'q} W_{1pn,\,2p'n'}^{1p+qn,\,2p'-qn'}\mathcal{P}, \tag{2}$$

where

$$\mathcal{P} = [F_{np}^{(1)}F_{n'p'}^{(2)}(1-F_{np+q}^{(1)})(1-F_{n'p'-q}^{(2)}) - F_{np+q}^{(1)}F_{n'p'-q}^{(2)}(1-F_{np}^{(1)})(1-F_{n'p'}^{(2)})]. \tag{3}$$

As in [1], we assume that the wires are different but have the same lengths L and consider the interaction processes when the scattered electrons in both nanowires remain within the initial subbands $\varepsilon_{np}^{(1)} = \varepsilon_n^{(1)}(0) + p^2/2m$ and $\varepsilon_{n'p}^{(2)} = \varepsilon_{n'}^{(2)}(0) + p^2/2m$, when n is the band number.

The first iteration of (1) gives for the nonequilibrium part of the distribution function $\Delta F_{np}^{(1)}$

$$\Delta F_{np}^{(1)} = -\left(z \pm \frac{L}{2}\right)\frac{1}{v_{np}}I^{(12)}\{F^{(1)}, F^{(2)}\} \tag{4}$$

for $p > 0$ and $p < 0$, respectively. Using the particle conservation property of the scattering integral

$$\sum_n \int dp I^{(12)}\{F^{(1)}, F^{(2)}\} = 0, \tag{5}$$

we get for the drag current

$$J = -2eL\sum_n \int_0^\infty \frac{dp}{2\pi\hbar} I^{(12)}\{F^{(1)}, F^{(2)}\}. \tag{6}$$

The scattering probability $W_{1pn,\,2p'n'}^{1p+qn,\,2p'-qn'}$ in (2) includes the delta-function which allows for the energy conservation for the electrons belonging to two different wires,

$$W_{1pn,\,2p'n'}^{1p+qn,\,2p'-qn'} = \frac{2\pi}{\hbar}\left|V_{1pn,\,2p'n'}^{1p+qn,\,2p'-qn'}\right|^2 \times \delta(\varepsilon_{np}^{(1)} + \varepsilon_{n'p'}^{(2)} - \varepsilon_{np+q}^{(1)} - \varepsilon_{n'p'-q}^{(2)}), \tag{7}$$

[1] This article was submitted by the authors in English.

[2] Some references to the early papers on the Coulomb drag are given in [1].

and which following [1] can be brought into the form

$$\delta(\varepsilon^{(1)}_{np} + \varepsilon^{(2)}_{n'p'} - \varepsilon^{(1)}_{np+q} - \varepsilon^{(2)}_{n'p'-q}) = \frac{m}{|p-p'|}\delta(q + p - p'). \quad (8)$$

This means that we deal with the backscattering processes when the electrons swap their quasimomenta as a result of collision.

To calculate the drag current, we use the first iteration in the collision term for the Boltzmann equation. One can insert the equilibrium distribution functions into the collision term, e.g., $F^{(1)}_{np} = f(\varepsilon^{(1)}_{np} - \mu)$ for the first wire, where $f(\varepsilon - \mu)$ is the Fermi function.

We assume, following the Landauer–Buttiker–Imry [3, 4] approach, that the driving quantum wire is connected to two reservoirs that we call "left" (l) and "right" (r), each of them being in independent equilibrium described by the shifted chemical potentials $\mu^{(l)} = \mu - eV/2$ and $\mu^{(r)} = \mu + eV/2$. In these expressions, μ is the average chemical potential, $\Delta\mu/e = V$ is the voltage across wire 2 (we assume that $eV > 0$), and $e < 0$ is the electron charge. Therefore, the electrons entering the wire from the "left" ("right") and having quasimomenta $p' > 0$ ($p' < 0$) are described by the functions

$$F^{(2)}_{n'p'} = f(\varepsilon^{(2)}_{n'p'} - \mu^{(l)}) \quad p' > 0,$$
$$F^{(2)}_{n'p'} = f(\varepsilon^{(2)}_{n'p'} - \mu^{(r)}) \quad p' < 0, \quad (9)$$

whence it follows that the collision integral (2), (3) is zero if the initial quasimomentum p' and the final quasimomentum $p' - q$ of an electron are of the same sign. In other words, only the backscattering processes occur; otherwise, the equilibrium distribution functions on the right-hand side of (2), (3) would depend on the same chemical potential and the collision term would vanish.

In virtue of (8), we are interested only in the $p' < 0$ values [because of the restriction $p' - q = p > 0$ that follows from (6)] and arrive at the following product of distribution functions in the collision term (2), (3)

$$\mathcal{P} = F^{(1)}_{np}F^{(2r)}_{n'p'}(1 - F^{(1)}_{np'})(1 - F^{(2l)}_{n'p}) - F^{(1)}_{np'}F^{(2l)}_{n'p}(1 - F^{(1)}_{np})(1 - F^{(2r)}_{n'p'}) \quad (10)$$

or

$$\mathcal{P} = f(\varepsilon^{(1)}_{np} - \mu) f(\varepsilon^{(2)}_{n'p'} - \mu^{(r)})[1 - f(\varepsilon^{(1)}_{np'} - \mu)] \times [1 - f(\varepsilon^{(2)}_{n'p} - \mu^{(l)})] - f(\varepsilon^{(1)}_{np'} - \mu) f(\varepsilon^{(2)}_{n'p} - \mu^{(l)}) \times [1 - f(\varepsilon^{(1)}_{np} - \mu)][1 - f(\varepsilon^{(2)}_{n'p'} - \mu^{(r)})]. \quad (11)$$

This expression can be recast in the form

$$\mathcal{P} = 2\sinh(eV/2k_BT)\exp\{(\varepsilon^{(1)}_{np} - \mu)/k_BT\} \times \exp\{(\varepsilon^{(2)}_{n'p'} - \mu)/k_BT\} f(\varepsilon^{(1)}_{np} - \mu) \times f(\varepsilon^{(2)}_{n'p'} - \mu - eV/2) f(\varepsilon^{(1)}_{np'} - \mu) f(\varepsilon^{(2)}_{n'p} - \mu + eV/2), \quad (12)$$

and for the drag current we have

$$J = -2e\sinh\left(\frac{eV}{2k_BT}\right)\frac{2\pi}{\hbar}\frac{mL}{2\pi\hbar}\left(\frac{2L}{2\pi\hbar}\right)^2\left(\frac{2e^2}{\kappa L}\right)^2 \times \sum_{nn'}\int_0^\infty dp \int_0^\infty dp' \frac{g_{nn'}(p + p')}{p + p'}\mathcal{Q}, \quad (13)$$

where

$$\mathcal{Q} = \exp\frac{\varepsilon^{(1)}_{np} - \mu}{2k_BT}\exp\frac{\varepsilon^{(2)}_{n'p'} - \mu}{2k_BT} f(\varepsilon^{(1)}_{np} - \mu) \times f\left(\varepsilon^{(2)}_{n'p'} - \mu - \frac{eV}{2}\right) f(\varepsilon^{(1)}_{np'} - \mu) f\left(\varepsilon^{(2)}_{n'p} - \mu + \frac{eV}{2}\right), \quad (14)$$

κ is the dielectric susceptibility of the sample, and

$$g_{nn'}(q) = [\int d\mathbf{r}_\perp \int d\mathbf{r}'_\perp |\phi_n(\mathbf{r}_\perp)|^2 K_0(|q||\mathbf{r}_\perp - \mathbf{r}'_\perp|/\hbar)|\phi_{n'}(\mathbf{r}'_\perp)|^2]^2. \quad (15)$$

Some estimates for this function are given in [1].

According to the considerations presented in [1], those terms in sum (13) in which the differences $|\varepsilon^{(1)}(0) - \varepsilon^{(2)}(0)|$ are much greater than both k_BT and eV do not contribute to the current J. Therefore, we have to deal only with the terms, for which $|\varepsilon^{(1)}(0) - \varepsilon^{(2)}(0)|$ is smaller than or of the order of k_BT or eV. We assume for simplicity that there is only one such difference (otherwise, we would deal with a sum of several terms of the same type).

Since $\mathcal{Q}$ is a sharp function of p and p', one can factor all slowly varying functions outside the integral sign to get

$$J = J_0\frac{1}{2}\sinh\left(\frac{eV}{2k_BT}\right) \times \frac{\frac{eV}{4k_BT} - \frac{\varepsilon_{nn'}}{2k_BT}}{\sinh\left(\frac{eV}{4k_BT} - \frac{\varepsilon_{nn'}}{2k_BT}\right)}\frac{\frac{eV}{4k_BT} + \frac{\varepsilon_{nn'}}{2k_BT}}{\sinh\left(\frac{eV}{4k_BT} + \frac{\varepsilon_{nn'}}{2k_BT}\right)}, \quad (16)$$

where

$$J_0 = -\frac{8e^5m^3L(k_BT)^2}{\kappa^2\pi^2\hbar^4}\frac{g_{nn'}(2p_n)}{p_n^3}. \quad (17)$$

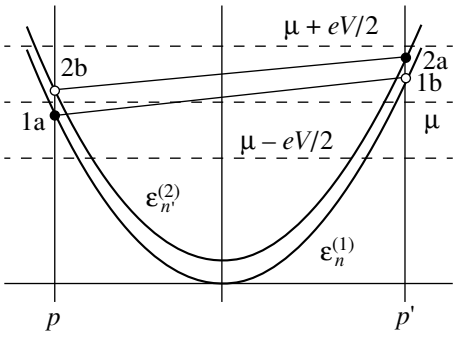

Fig. 1. Schematic representation of the simultaneous transitions caused by the interaction between electrons of two wires at $eV \gg k_B T$. Circles ○ and ● represent the initially unoccupied and occupied states, respectively.

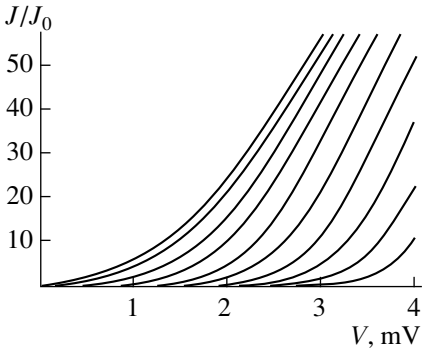

Fig. 2. Dependence of the drag current on the driving voltage for $T = 1$ K. The values of $|\varepsilon_{nn'}|$ increase from left to right.

Here, we introduce notations

$$\varepsilon_{nn'} = \varepsilon_n^{(1)}(0) - \varepsilon_{n'}^{(2)}(0),$$

$$m v_n = p_n = \sqrt{2m[\mu - \varepsilon_n^{(1)}(0)]}\ .$$

Let us make an order-of-magnitude estimate for the drag current J in a realistic situation. We assume that $T = 1$ K, $\mu = 14$ meV, the widths of the wires are 25 nm, the distance between the central lines of the wires is 50 nm, $\kappa = 13$, and $m = 6.7 \times 10^{-29}$. Then,

$$J_0 \approx 10^{-10}\ \text{A}. \tag{18}$$

For $eV \ll k_B T$, (16) coincides with the result obtained in [1]. Let us consider in detail the opposite case of $eV \gg k_B T$. In this case, result (16) does not vanishing only if $|\varepsilon_{nn'}| < eV/2$, and one obtains the following equation for the drag current:

$$J = \mathcal{B}\left[\left(\frac{eV}{2}\right)^2 - (\varepsilon_{nn'})^2\right],$$
$$\mathcal{B} = -\frac{2e^5 m^3 L}{\kappa^2 \pi^2 \hbar^4} \frac{g_{nn'}(2p_n)}{p_n^3}. \tag{19}$$

The situation is illustrated in Fig. 1. The straight lines correspond to the chemical potentials $\mu^{(r)}$ and $\mu^{(l)}$, and the middle dashed line corresponds to the average μ value. Parabolas 1 and 2 represent the dispersion laws for electrons in wires 1 and 2, respectively. The full circles correspond to the initial states of colliding electrons.

Before the collision, states 1a and 2a are occupied. The circle representing state 1a lies below the dashed line, i.e., below the Fermi level μ. The circle 2a represents a state with $p > 0$ that is also occupied because the corresponding energy is lower than $\mu^{(r)}$.

After the collision, state 1b is occupied. It is represented by a circle above the dashed line, indicating that it was unoccupied before the collision. In wire 2, state 2b with $p < 0$ is also occupied. It lies above $\mu^{(l)}$; i.e., it was vacant before the transition.

The width of the stripe between the two straight lines is equal to eV. The drag current should be proportional to the number of the occupied initial states and the number of free final states. As a result, we have for $eV \gg |\varepsilon_{nn'}|$: $J \propto V^2$ (see Fig. 2).

In summary, we developed the theory of Coulomb drag current induced in a quantum wire by a nonohmic current in a nearby parallel nanowire. A ballistic transport in both nanowires is assumed. The drag current J as a function of the gate voltage exhibits a system of spikes, with the position of each spike being determined by the coincidence of a pair of transverse quantization levels, $\varepsilon_n(0)$ and $\varepsilon_{n'}(0)$ in both wires. At $eV \gg k_B T$, J is a parabolic function of the driving voltage V. The effect may play an important role in the investigation of the interwire Coulomb scattering, as well as 1D band structure of wires.

ACKNOWLEDGMENTS

We are grateful to P. Debray for sending a preprint of paper [2] prior to publication. This work was supported by the Russian Foundation for Basic Research, project no. 97-02-18286-a.

REFERENCES

1. V. L. Gurevich, V. B. Pevzner, and E. W. Fenton, J. Phys.: Condens. Matter **10**, 2551 (1998).
2. P. Debray, P. Vasilopulos, O. Raĭchev, *et al.* (in press).
3. R. Landauer, IBM J. Res. Dev. **1**, 233 (1957); **32**, 306 (1988).
4. Y. Imry, *Directions in Condensed Matter Physics*, Ed. by G. Grinstein and G. Mazenko (World Scientific, Singapore, 1986), p. 101; M. Büttiker, Phys. Rev. Lett. **57**, 1761 (1986).

JETP Letters, Vol. 71, No. 3, 2000, pp. 114–116. Translated from Pis'ma v Zhurnal Éksperimental'noĭ i Teoreticheskoĭ Fiziki, Vol. 71, No. 3, 2000, pp. 169–173.

CONDENSED MATTER

Effects of Pressure and Magnetic Field on the Electrical Resistivity of $La_{0.8}Ba_{0.2}MnO_3$ in Rhombohedral and Orthorhombic Phases

V. E. Arkhipov*, V. S. Gaviko*, K. M. Demchuk*, V. P. Dyakina*, A. V. Korolev*, Ya. M. Mukovskiĭ, É. A. Neĭfel'd*, and R. V. Pomortsev*[1]**

** Institute of Metal Physics, Ural Division, Russian Academy of Sciences, Yekaterinburg, 620219 Russia*

*** Moscow Institute of Steel and Alloys, Moscow, 117939 Russia*

Received December 30, 1999

Abstract—A structural transition from the orthorhombic phase to the rhombohedral one is observed and investigated on a $La_{0.8}Ba_{0.2}MnO_3$ single crystal. In the region of the coexistence of two phases, the effects of magnetic field (up to 12 T) and hydrostatic pressure (up to 5 kbar) on the temperature dependences of the electrical resistivity are studied. It is shown that magnetic field and pressure reduce the transition temperature and produce qualitatively similar effects on the electrical resistivity in the region of the structural transition. *© 2000 MAIK "Nauka/Interperiodica".*

PACS numbers: 72.15.Gd; 72.60+g; 61.50.Ks

This paper presents the results of X-ray diffraction studies of the $La_{0.8}Ba_{0.2}MnO_3$ compound in the temperature range 80–300 K and the studies of the dependences of its electrical resistivity on magnetic field and pressure in the temperature range 160–200 K within which a first-order structural phase transition was observed.

The samples were cut out of a $La_{0.8}Ba_{0.2}MnO_3$ single crystal grown by the floating zone method with the zone heating by xenon lamp radiation. The galvanomagnetic properties were studied using the four-probe dc technique. The measurements under hydrostatic pressure were performed in a high-pressure cell filled with helium, which served as the pressure-transmitting medium. In addition to the aforementioned properties, for a more complete characterization of the system under study, we measured the thermo-emf, which was found to be ≈8 μV/K at 300 K and ≈–7 μV/K at 30 K. The change of sign of the thermo-emf occurred at $T \approx$ 240 K.

The crystal structure and the phase composition of the samples were studied by a DRON automated X-ray diffractometer (with monochromatic CrK_α-radiation) on powder specimens made of the single crystal.

Figure 1 presents the temperature dependences of the lattice parameters of $La_{0.8}Ba_{0.2}MnO_3$. In the temperature range $80 < T < 185$ K, the diffraction patterns display the diffraction lines of only the orthorhombic *Pbnm* phase. At 185 K, along with the reflections from the orthorhombic phase, weak diffraction lines of the rhombohedral $R\bar{3}c$ phase become visible. With increasing temperature, the relative intensity of the lines of the $R\bar{3}c$ phase increases, while the intensity of the lines of the *Pbnm* phase decreases; above T = 196 K, the latter lines virtually disappear. The manner in which the reflections from the rhombohedral phase appear in the diffraction pattern and the presence of a two-phase region testify that the phase transition observed in $La_{0.8}Ba_{0.2}MnO_3$ is a first-order one. The orthorhombic-to-rhombohedral structural transition, which occurs with increasing temperature, is accompanied by a decrease in the unit cell volume. The decrease in the volume per unit formula is ≈0.65%.

Figure 2 shows the temperature dependences of the resistivity in magnetic fields H = 0, 5 and 12 T in the temperature range 175–210 K; the dependences were obtained for both heating and cooling of the sample. In the temperature region corresponding to the structural phase transition, a pronounced temperature hysteresis is visible. With increasing magnetic field, the hysteresis loop shifts toward lower temperatures, and the difference between the electrical resistivities of the low-temperature and high-temperature phases decreases. We note that a similar structural transition was observed in $La_{0.88}Sr_{0.12}MnO_3$ at T = 145 K: in the ferromagnetic state, this material developed a transition from the orthorhombic phase to the pseudocubic one [1]. In the same experiment, concurrently with the structural transition, a metal-to-dielectric transition was observed with both the transition temperature and the magnitude of the electrical resistivity drop depending on the external magnetic field.

[1] E-mail: pomor@imp.uran.ru

0021-3640/00/7103-0114$20.00

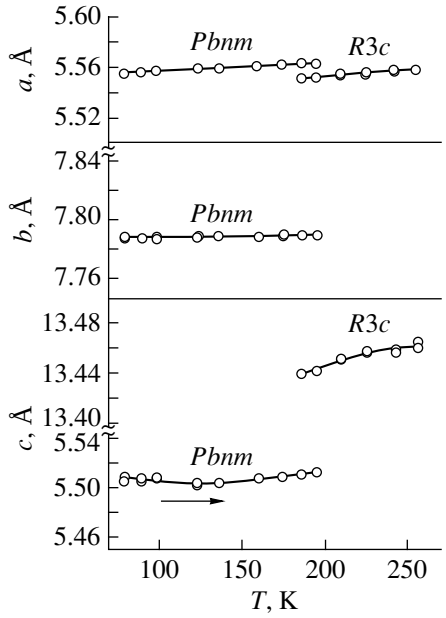

Fig. 1. Temperature dependences of the lattice parameters of $La_{0.8}Ba_{0.2}MnO_3$.

Figure 3 presents the temperature dependences of the electrical resistivity under hydrostatic pressure. With increasing pressure, the hysteresis loop shifts toward lower temperatures, and the difference between the resistivities of the low-temperature and high-temperature phases decreases, which is similar to the behavior of the resistivity in magnetic field.

In lanthanum manganites with perovskite structure, the manganese ions are positioned at the centers of the octahedra, which have oxygen ions at their vertices; sharing their vertices, the octahedra form the spatial lattice. The trivalent lanthanum ions La^{3+} and the substitutional divalent ions of the doping element are located in the space between the MnO_6 octahedra. The electronic configuration of a trivalent manganese ion Mn^{3+} is $3d^4$. If Hund's intra-atomic splitting is large, the electronic configuration of a Mn^{3+} ion will be $t_{2g}^3 e_g$. The t_{2g}-state electrons are localized and form a magnetic moment ($S = 3/2$). The e_g-state electrons being strongly hybridized with the oxygen $2p$ states form the conduction band with hole-type carriers, which result from the substitution of divalent elements for La^{3+} ions [2–5].

In the double-exchange model [4, 5], the matrix element t_{ij} describing the carrier transfer between the sites i and j occupied by manganese ions has the form $t_{ij} = t\cos(\theta/2)$, where θ is the angle between the magnetic moments S_i and S_j localized at the sites i and j. The quantity t characterizes the degree of overlapping of the wave functions describing the corresponding states of the sites between which the hopping occurs. Because of the strong hybridization of the manganese e_g states and the oxygen $2p$ states, the quantity t depends on the Mn–O–Mn bond angle φ, which in cubic perovskite compounds is equal to 180°.

In lanthanum manganites, the deviation of the angle φ from 180° is determined by the relative values of the effective radii of the trivalent lanthanum, the substitutional divalent element, and the Mn^{3+} and Mn^{4+} ions. Therefore, the angle φ depends not only on the composition but also on the doping level [6].

The value of the Mn–O–Mn bond angle can be efficiently varied by applying external hydrostatic pressure [5]. Without affecting the composition and the effective radii of the ions, external pressure leads to a decrease in the interatomic distances. As a result, the MnO_6 octahedron begins to unfold. In systems with a perovskite structure, an increase in pressure leads to an increase in

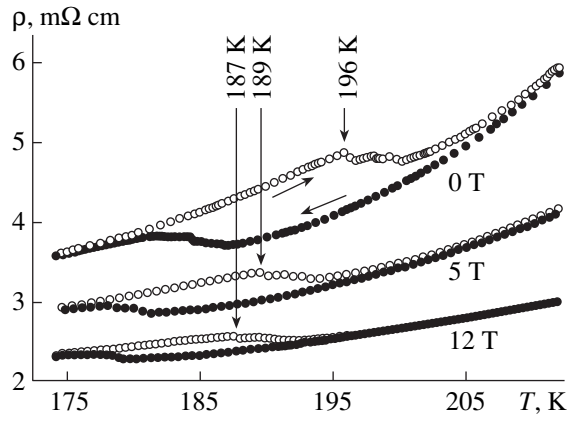

Fig. 2. Temperature dependences of the electrical resistivity of $La_{0.8}Ba_{0.2}MnO_3$ in magnetic fields 0, 5, and 12 T.

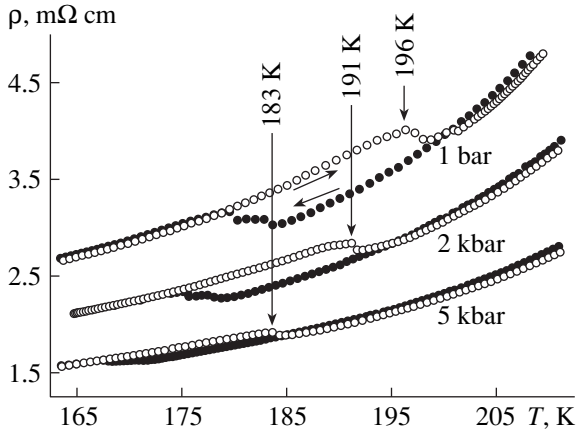

Fig. 3. Temperature dependences of the electrical resistivity of $La_{0.8}Ba_{0.2}MnO_3$ under hydrostatic pressure of 1 bar and 2 and 5 kbar.

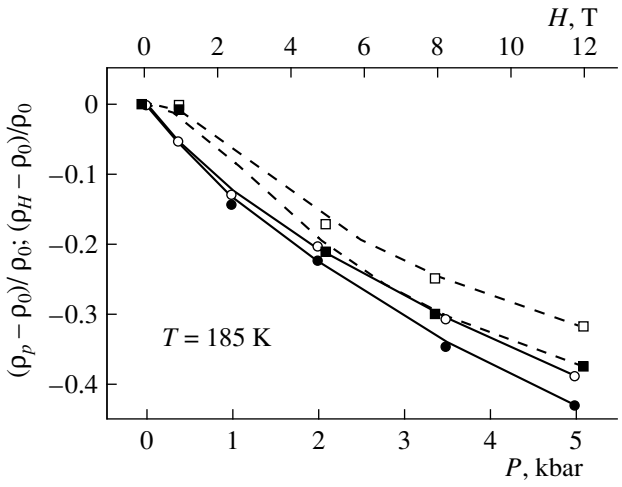

Fig. 4. Dependences of the electrical resistivity on (solid curves) pressure and (dashed curves) magnetic field for the (□ and ■) orthorhombic and (○ and ●) rhombohedral phases at $T = 185$ K.

the angle φ. In the mean ligand field approximation, the transfer matrix element t is proportional to $\cos(\pi - \varphi)$; therefore, as the angle φ increases approaching 180°, the matrix element t increases [5]. Since the conduction bandwidth is approximately proportional to t^2, the external pressure leads to its increase and, hence, to a decrease in the resistivity.

Figure 4 shows the pressure dependences of the quantity $(\rho_p - \rho_0)/\rho_0$ for the high-temperature and low-temperature phases at $T = 185$ K. Here, ρ_p is the electrical resistivity under pressure and ρ_0 is the resistivity at $P = 1$ bar and $H = 0$. One can see that, with increasing pressure, the electrical resistivity of the low-temperature (orthorhombic) phase decreases faster than the resistivity of the high-temperature (rhombohedral) phase. At $P = 5$ kbar, the difference in the resistivities reaches ≈10%. Since the decrease in the resistivity with pressure can be mainly attributed to the increase in the Mn–O–Mn bond angle, the results of our measurements testify that the variation of the angle φ with increasing pressure occurs faster in the orthorhombic phase than in the rhombohedral one. The same figure presents the dependence of the magnetoresistance $\Delta\rho/\rho$ on magnetic field for both phases at $T = 185$ K. One can see that the orthorhombic phase is characterized by greater values of magnetoresistance as compared to the rhombohedral phase. At $H = 12$ T, this difference reaches ≈17%.

From Figs. 2 and 3, it follows that, in the temperature range studied in the experiment, both phases exhibit a metal-like electrical conduction ($d\rho/dT > 0$), and their resistivity is $\approx 3 \times 10^3$ μΩcm at $H = 0$. This value is close to the Mott resistivity limit ρ_{max}, which for $La_{0.8}Ba_{0.2}MnO_3$ lies within the interval $(5 - 10) \times 10^3$ μΩcm. Thus, in terms of the electrophysical properties, in the temperature range $175 < T < 210$ K, both phases of $La_{0.8}Ba_{0.2}MnO_3$ are poor metals whose density of states in the vicinity of the Fermi level is low and weakly depends on energy. This conclusion is strengthened, firstly, by the value of the thermo-emf, which, as was mentioned above, is small and weakly temperature-dependent, and, secondly, by the qualitatively similar dependences of the resistivities of the two phases on magnetic field and pressure.

ACKNOWLEDGMENTS

This work was supported by the Russian Foundation for Basic Research, project no. 99-02-16280.

REFERENCES

1. Y. Endoh, H. Nojiri, K. Kaneko, *et al.*, Mater. Sci. Eng. B **63**, 151 (1999).
2. C. Zener, Phys. Rev. **82**, 403 (1951).
3. P. G. de Gennes, Phys. Rev. **118**, 141 (1960).
4. A. P. Ramírez, J. Phys.: Condens. Matter **9**, 8171 (1997).
5. M. Imada, A. Fujimori, and Y. Tokura, Rev. Mod. Phys. **70**, 1039 (1998).
6. R. Mahendiran, S. K. Tiwary, A. K. Raychaudhuri, *et al.*, Phys. Rev. B **53**, 3348 (1996).

Translated by E. Golyamina

JETP Letters, Vol. 71, No. 3, 2000, pp. 117–122. Translated from Pis'ma v Zhurnal Éksperimental'noĭ i Teoreticheskoĭ Fiziki, Vol. 71, No. 3, 2000, pp. 174–181.

CONDENSED MATTER

Collective Behavior of Interwell Excitons in GaAs/AlGaAs Double Quantum Wells

A. V. Larionov*, V. B. Timofeev*[1], J. Hvam, and C. Soerensen****

** Institute of Solid State Physics, Russian Academy of Sciences, Chernogolovka, Moscow oblast, 142432 Russia*

*** Microelectronic Center, DK 2800 Lyngby, Denmark*

Received December 30, 1999

Abstract—Photoluminescence spectra of interwell excitons in double GaAs/AlGaAs quantum wells (*n–i–n* structures) have been investigated (an interwell exciton in these systems is an electron–hole pair spatially separated by a narrow AlAs barrier). Under resonance excitation by circularly polarized light, the luminescence line of interwell excitons exhibits a significant narrowing and a drastic increase in the degree of circular polarization of photoluminescence with increasing exciton concentration. It is found that the radiative recombination rate significantly increases under these conditions. This phenomenon is observed at temperatures lower than the critical point and can be interpreted in terms of the collective behavior of interwell excitons. © *2000 MAIK "Nauka/Interperiodica".*

PACS numbers: 73.20.Mf; 73.20.Dx; 78.55.Cr

1. Tunneling quantum systems (superlattices and double quantum wells) have long been the subjects of intensive studies [1–8]. In principle, electron and hole charge carriers can be spatially separated in these two-dimensional systems, which is the reason for this interest. In double quantum wells with an applied band-declining electric displacement, one can excite excitons with the electron and the hole located in different quantum wells separated by a tunnel-transparent barrier. Such excitons are named spatially indirect (I) or interwell excitons, as distinct from direct intrawell excitons, in which the electron and the hole are located in the same quantum well. Interwell excitons are long-lived as compared to intrawell excitons. Therefore, these excitons can easily be accumulated, and the gas of such excitons can be cooled down to rather low temperatures. Because the central symmetry is broken, interwell excitons have a dipole moment already in the ground state. Theory predicts various possible scenarios of the collective behavior in a system of spatially separated electrons and holes [1, 9–14]. Thus, in the recent work [14], it was shown that a liquid dielectric phase of such excitons could be a stable state of the electron–hole system at certain critical parameters (the dipole moment of interwell excitons, their density, and temperature) in spite of the dipole–dipole repulsion of interwell excitons. Previously, it was indicated [11] that a condensed dielectric excitonic phase can occur only in the case of lateral confinement (accidental or artificially prepared) in the quantum well plane. This confinement and the related external compression allow rather large densities to be achieved in the gas of interwell excitons.

A random potential due to diverse structural defects (residual charged and neutral impurities, fluctuations of the barrier width and the widths of the interwell excitons themselves, etc.) is always present in the real tunneling quantum systems based on semiconductor heterostructures. These fluctuations generate a random potential profile in quantum well planes. Therefore, photoexcited electrons and holes spatially separated between neighboring quantum wells, as well as excitons, become strongly localized in the regions of these fluctuations at sufficiently low temperatures. This localization effect in coupled quantum systems is, in particular, manifested in the lateral, thermally activated tunneling of charge carriers and is revealed in experiments on spectral narrowing of the luminescence line corresponding to interwell radiative recombination with increasing temperature [7].

This work is devoted to studying the photoluminescence of interwell excitons in a double quantum well with the barrier separating the quantum wells that contains four AlAs monolayers. When the barriers are so narrow, interwell excitons are rather strongly bound. In this case, if the linear scale of fluctuations $l > a_B$ (the exciton Bohr radius is about $a_B \leq 100$ Å) and the amplitude of fluctuations $\Delta > kT$, interwell excitons are to be localized at lateral fluctuations of the random potential without changing significantly their internal structure. It is known that the barrier width in structures with narrow AlAs barriers is characterized by large-scale fluctuations. Therefore, the lateral potential barrier will also be characterized by large-scale fluctuations. It is

[1] E-mail: timofeev@issp.ac.ru

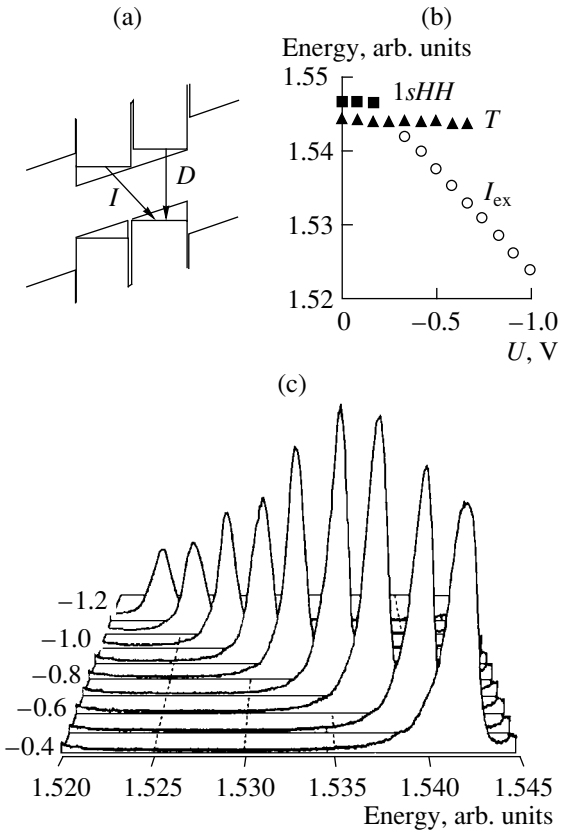

Fig. 1. (a) Schematic diagram of optical transitions; (b) spectral positions of lines of the direct exciton (1*sHH*), the excitonic complex (*T*), and interwell excitons (I_{ex}) as a function of the electric displacement; and (c) the behavior of luminescence spectra of interwell excitons as a function of the applied voltage (numbers on the right of the spectra correspond to the electric voltage in volts) at $T = 2$ K.

reasonable to expect that interwell excitons at sufficiently low temperatures will reside in such accidental lateral large-scale potential wells. It is interesting to know whether the system of excitons under conditions of such accidental lateral confinement will exhibit critical behavior when the density increases at low temperatures. In this work, we attempt to answer the above questions.

2. We investigated an *n–i–n* GaAs/AlGaAs heterostructure with a double quantum well GaAs/AlAs/GaAs (the width of GaAs wells is about 120 Å, and the width of the AlAs barrier is about 11 Å). The structure was grown using molecular-beam epitaxy on an *n*-type doped GaAs support (the concentration of the doping Si: impurity was 10^{18} cm^{-3}) with the (001) crystallographic orientation. First, a 0.5-μm buffer layer of Si-doped (10^{18} cm^{-3}) GaAs was grown on the support. Next, an insulating AlGaAs layer ($x = 0.33$) with a thickness of 0.15 μm was put in place. Next, GaAs/AlAs/GaAs double quantum wells were grown. After the double quantum well, an insulating AlGaAs layer with a thickness of 0.15 μm was put in place, followed by a 0.1-μm layer of Si-doped (10^{18} cm^{-3}) GaAs. The whole structure was covered by a 100-Å GaAs layer. Mesas of size 1×1 mm^2 were made on the structure by the lithographic method. Metallic contacts of an Au + Ge + Pt alloy were applied to the buffer layer and to the doped layer in the upper part of a mesa.

Luminescence spectra were investigated under conditions of resonance excitation of intrawell direct heavy-hole excitons with the use of a tunable Ti-sapphire laser. With the aim of optically orienting the angular momentum of the exciton, we used circularly polarized resonance excitation. The kinetics of luminescence spectra was studied under pulse excitation by a picosecond laser (wavelength 6200 Å, pulse duration 30 ps, and pulse frequency 0.8 MHz). The time evolution of spectra and the kinetics of intensities were measured using a system of time-correlated single-photon counting.

3.1. Figure 1c demonstrates the luminescence spectra of interwell excitons (I_{ex}) measured under resonance excitation of the 1*sHH* exciton and at various applied electric displacements. Two lines are observed in the region of intrawell luminescence at a zero electric displacement: the line 1*sHH* of the free exciton and the line *T* of the bound exciton. At a negative electric displacement, starting from –0.4 V, the spectra exhibit a line of interwell radiative recombination, which linearly shifts toward lower energies as the applied voltage increases (see Fig. 1b). In this case, only the line of the charged excitonic complex *T* remains in the spectrum of intrawell recombination [15]. At large negative displacements $U < -0.8$ V and stationary excitation, only the luminescence line of the interwell exciton remains detectable in the spectra, whereas the luminescence of direct intrawell excitons and excitonic complexes is several orders of magnitude weaker in intensity. The intensity of the interwell-exciton line behaves as a nonmonotonic function of the applied negative displacement. This line appears in the luminescence spectrum at such electric displacements when the Stark shift exceeds the difference of binding energies of the intrawell and interwell excitons, $eFz \geq E_D - E_I$. At $U \sim -0.7$ V, the intensity of this line is a maximum and then monotonically drops with increasing electric field (see Fig. 1c). This behavior can easily be understood with regard to the fact that, as the field increases, the effective dipole moment of the interwell exciton increases in the direction of structure growth (*z*-axis). In this case, the overlap between the wave functions of the electron and the hole in the exciton monotonically decreases.

3.2. The luminescence line of the interwell exciton at sufficiently low temperatures ($T = 2$ K) and small pumping intensities has a large width (FWHM = 4–5 meV), and the line shape is asymmetric with a rather extended long-wavelength tail and a relatively sharp violet edge (see Fig. 2). These features of the photoluminescence line of interwell excitons are the

consequences of their strong localization in the regions of fluctuations of the random potential. In this case, the line width reflects the statistical distribution of amplitudes of the random potential (it is implied that the pumping is so small, $n_{e-h} < 10^9$ cm^{-2}, that the occupation of accidental potential wells with linear scales $l < 1$ μm does not exceed one).

The luminescence line width and shape of interwell excitons significantly change with increasing power of the resonance excitation of direct 1*sHH* intrawell excitons by circularly polarized light (see Fig. 2). With increasing pumping, line *I* is narrowed down to 1.5 meV, that is, more than three times. The narrowing of the line is accompanied by a strong superlinear increase in its intensity (see the inset in Fig. 2). Only at high pumping intensities ($P > 6$ W/cm^2) does this line shift toward high energies and somewhat broaden. The line shift toward high energies indicates that the applied electric field is screened when the interwell-exciton density becomes sufficiently large. From here, the interwell-exciton density can be estimated from the above when the luminescence line width reaches its minimum. This estimation gives $n = 3 \times 10^{10}$ cm^{-2} for the concentration. We observed a significant narrowing of the luminescence line of interwell excitons at various applied negative displacement voltages from –0.5 V to –1.2 V. At large negative displacements, the narrowing of the luminescence line of interwell excitons occurred at considerably lower pumping intensities.

3.3. Of interest is the behavior of the degree of circular polarization γ of the interwell-exciton line with increasing power of resonance excitation (see the inset in Fig. 2). Direct, 1*sHH*, fully spin-oriented excitons ($J_h = +3/2$ and $S_z = -1/2$) were generated in our experiments on resonance excitation by circularly polarized light. Because of the tunneling of carriers, their binding into interwell excitons, spin–lattice relaxation, and strong spin–orbit interaction of holes, the spin memory of interwell excitons is partially lost but, nevertheless, remains high and comprises almost 15–20% at a low excitation density. When the power of resonance excitation increases so that the luminescence line of interwell excitons becomes strongly narrowed, the degree of circular polarization of the corresponding line increases more than two times. If it is suggested that the spin relaxation rate τ_s varies only slightly with increasing pumping intensity (most likely, it can only increase), then the increase in the degree of circular polarization can be naturally associated with the decrease in the lifetime τ_d of interwell excitons. This follows from the simple kinetic equation relating the degree of circular polarization with the lifetime and the spin relaxation time $\gamma = \gamma_0/(1 + \tau_d/\tau_s)$ [16]. A threshold increase in the circular polarization of the narrow photoluminescence line of interwell excitons with increasing pumping was observed at resonance excitation by linearly polarized light (polarization was parallel to the plane of layers). When the excitation densities were not high and interwell excitons were strongly localized in the regions of fluctuations of the random potential, the photoluminescence spectra remained fully depolarized under such conditions. The details of experiments with linearly polarized excitation will be published separately.

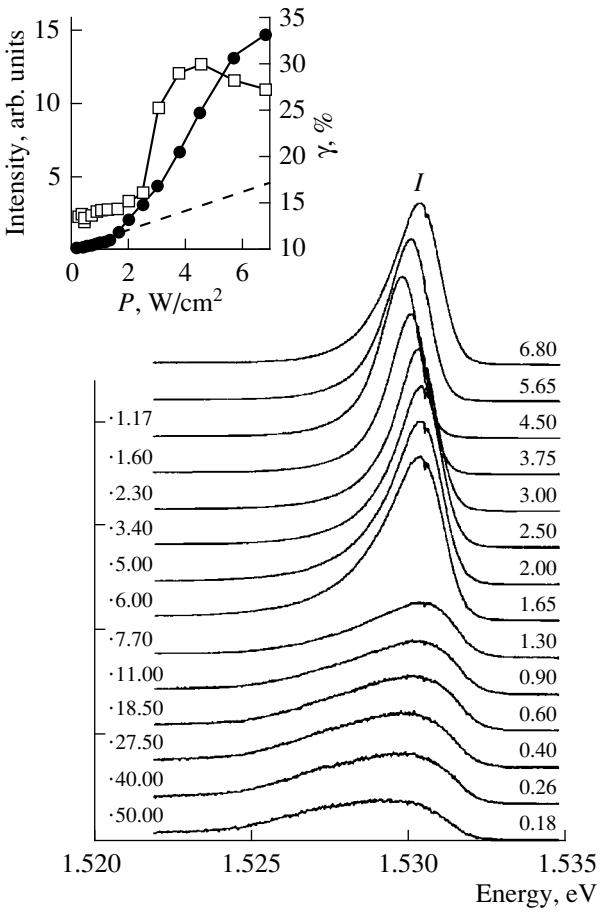

Fig. 2. Photoluminescence spectra of interwell excitons (line *I*) at various powers of the resonance excitation of the direct 1*sHH* exciton by circularly polarized light (σ^+), applied displacement –1 V, and $T = 2$ K. Numbers on the right of the spectra correspond to pumping intensities in W/cm^2, those on the left correspond to the scale factors in respect to the two upper spectra. The inset presents the line intensity of interwell excitons (round symbols, left scale) and its degree of circular polarization (square symbols, right scale) as functions of the power density. The dashed line is an extrapolation of the linear dependence of the intensity.

Thus, with increasing concentration of interwell excitons, the corresponding photoluminescence line is narrowed down and the degree of its polarization increases, which gives indirect evidence that the radiative decay time shortens. This phenomenon turned out to be very sensitive to temperature. At temperatures higher than critical values and fixed large pumping intensities, the line width of interwell excitons increases abruptly and the degree of circular polariza-

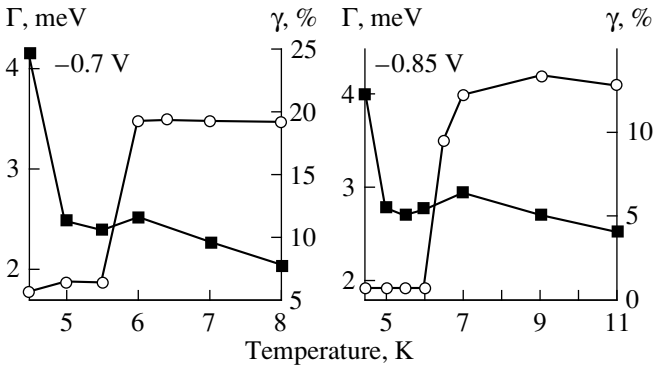

Fig. 3. Temperature dependence of the luminescence line width of interwell excitons Γ (round symbols, left scale) and its degree of circular polarization γ (square symbols, right scale) for electric displacements of –0.7 and –0.85 V.

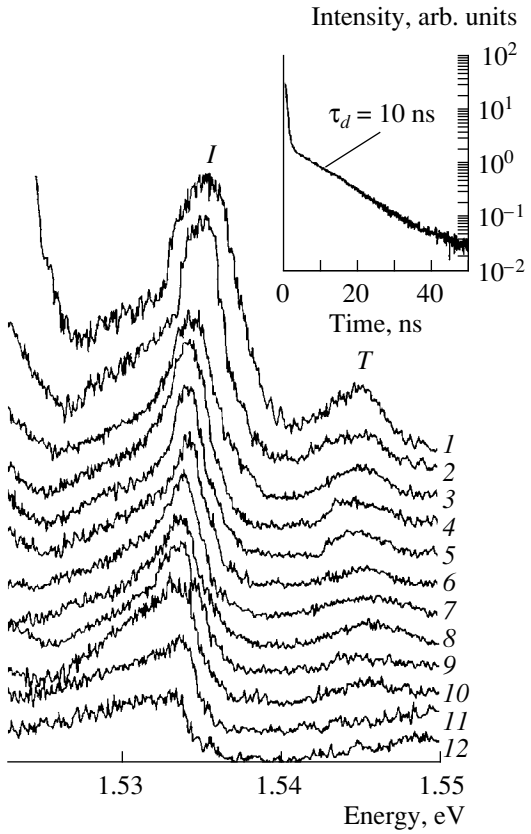

Fig. 4. Time evolution of spectra and the kinetics of the luminescence decay of interwell excitons (see inset) under conditions of pulse excitation at T = 5 K and displacement –0.7 V. Spectra *1–8* were measured with time delays of 2, 3, 4, 5, 6, 7, 8, and 10 ns and integration for 2 ns. Spectra *9–12* correspond to delays of 12, 16, 20, and 25 ns and integration for 4, 4, 5, and 6 ns, respectively. The intensity decay time of the narrow line of interwell excitons τ_d = 10 ns.

tion decreases down to previous values (see Fig. 3). In this case, the critical temperature at which such dramatic spectral changes were observed was $T_c \le 6$ K (ΔT = ±1 K).

3.4. We investigated the kinetics of photoluminescence spectra under conditions of pulse excitation with the use of a picosecond laser. Under this excitation, hot photoexcited electrons and holes are generated at the instant of laser pulse action in each quantum well with the same density and are not spatially separated. Figure 4 presents the time evolution of spectra under pulse excitation. The spectra were measured with different time delays in reference to the exciting laser pulse at T = 5 K and the applied voltage U = –0.7 V. At zero delays, only the region of direct intrawell luminescence is observed in the spectra. The photoluminescence spectrum of interwell excitons is formed at delays $\tau \ge 2$ ns. This delay is a consequence of carrier tunneling through the barrier accompanied by spatial separation of charge carriers among quantum wells; their intrawell energy relaxation; and, simultaneously, recombination. Figure 4 demonstrates that a sufficiently narrow line dominates at the violet edge of interwell photoluminescence spectra at small delays (<10 ns). With increasing delay, this line is significantly narrowed. Its width reaches 1.5 meV at a delay of 6 ns; that is, it decreases almost three times in comparison with its width at initial delays. The intensity of this line decays with time much faster than the structureless spectrum of interwell luminescence beneath it. At delays longer than 20 ns, this line is not resolved and blends into the structureless part of the spectrum, which remains almost unchanged in its shape and is observed at delays longer than 40 ns. This behavior is clearly evident in the kinetics of intensities measured directly at the spectral position of the narrow line (see the inset in Fig. 4). It is essential to note that the narrow band distinguished by the short-term kinetics of intensity decay under conditions of pulse excitation is observed, as well as in the case of stationary excitation, only at sufficiently low temperatures. Thus, in the case of delays of 12 ns, the narrow line starts to broaden and blends into the structureless background beneath it at $T \ge 6$ K. At shorter delays and, hence, at a higher density of interwell excitons, this line disappears in the spectrum at distinctly higher temperatures. For example, at a delay of 7 ns, the narrow line disappears in the spectra at $T \ge 10$ K. We observed the same behavior of the time-resolved spectra and kinetics of interwell luminescence at various applied voltages in the range from –0.4 to –0.9 V.

4. The totality of the experimental results presented above cannot be explained within the simple one-particle description of radiative annihilation of interwell excitons localized at fluctuations of the random potential. Thus, the appearance of the narrow line in the photoluminescence spectrum can be associated with delocalized interwell excitons, which appear above the percolation threshold. However, in this case, it remains completely inexplicable why this phenomenon is so sensitive to temperature and is not observed at $T > T_c$. The threshold increase of the degree of circular polarization and the superlinear growth of the intensity of

this line also remains unclear. At the same time, these results can be explained, at least, qualitatively as the consequence of the collective behavior of delocalized interwell excitons upon attaining the critical temperature and concentration. It can be suggested that the investigated structures with a narrow AlAs barrier are characterized by large-scale fluctuations of the potential, in particular, by those due to variations of the barrier width. Such fluctuations of the potential are poorly screened, as distinct from the random potential due to residual charged impurities, which also arises in the studied structures. Because of large-scale fluctuations of the potential profile in the plane of the quantum well, photoexcited interwell excitons can accumulate in macroscopically large areas with lateral confinement up to several tenths of a micron. It is in these areas that the main events associated with photoexcited interwell excitons proceed. These events can develop by independent scenarios, but collective interaction in the system of interwell excitons delocalized within macroscopically large lateral areas is suggested in the basis of each of them. Within one of the scenarios, it can be suggested that interwell excitons are condensed into a metallic *e–h* liquid with spatially separated electron–hole layers upon attaining the critical densities and temperature. If one associates the narrow line in the spectrum with the emerging liquid phase, then its density can be easily estimated from the above by the line width, which, in this case, must equal the sum of Fermi energies of electrons and holes. The density determined in this way equals 3×10^{10} cm^{-2}, and the dimensionless parameter r_s corresponding to this density equals $r_s = 1/\sqrt{\pi n a_B^2} = 4$. The condensed phase within this approach turns out to be too loose to shield completely the Coulomb interaction in interwell excitons; that is, excitons at these concentrations must retain their individuality. Therefore, the condensed phase cannot be metallic. This conclusion is confirmed by studies of photoluminescence spectra in a magnetic field with the Faraday geometry. It was found that the narrow line, similar to a free exciton, is split into a Zeeman doublet with the intensity ratio of components σ^+/σ^- corresponding to the temperature and the spin splitting value. That is, the individual properties of the exciton are retained in the condensed phase. The details of these experiments will be described in a separate publication.

We suggest that the effect of strong narrowing of the photoluminescence line of interwell excitons and the critical character of this phenomenon with respect to density and temperature can be associated with the condensation of interwell excitons into a dielectric liquid. It was shown in [14] that, at certain values of the dipole moment of interwell excitons, a sufficiently dense system of interwell excitons could condense into a dielectric liquid in spite of the dipole–dipole repulsion between such excitons. It was indicated in [11] that this condensation could most likely occur in the regions with lateral confinement. According to our experiments, under stationary excitation, the condensation occurs at $T < 6$ K and at an average exciton concentration of 3×10^{10} cm^{-2}.

The condensed part of excitons must be phased within the coherent length. Spatial coherence must occur at least at scales of the de Broglie wavelength of interwell excitons λ_{ex}, which equals $\lambda_{ex} = h/\sqrt{\pi m k T} = 1.5 \times 10^3$ Å at $T = 2$ K and exceeds the exciton Bohr radius by more than an order of magnitude. At the same conditions, the dimensionless parameter $r = n \times \lambda_{ex}^2 = 4$. The observed threshold increase of the circular polarization of interwell excitons gives indirect evidence of an increase of spatial coherence in the condensed phase. Furthermore, the radiative decay of phase-correlated interwell excitons in the condensate must be distinguished by considerably larger radiative probabilities, as compared to the photoluminescence of excitons beyond the condensate. This conclusion also agrees with the experiment.

Nevertheless, an essential question in justifying the assumption of the condensation of interwell excitons into a dielectric liquid phase remains open and requires an experimental answer. This question concerns the determination of the linear scales of spatial coherence. This problem can be solved experimentally, in particular, by measuring intensity correlations under conditions when the suggested exciton condensation occurs.

ACKNOWLEDGMENTS

The authors are grateful to V.F. Gantmakher, S.V. Iordanskiĭ, A.S. Ioselevich, V.D. Kulakovskiĭ, Yu.E. Lozovik, V.G. Lysenko, and R.A. Suris for interesting discussions. This work was in part supported by the Russian Foundation for Basic Research, project no. 98-02-16656, and by the interdepartmental program "Nanostructures."

REFERENCES

1. E. Yu. Lozovik and V. I. Yudson, Zh. Éksp. Teor. Fiz. **71**, 738 (1976) [Sov. Phys. JETP **44**, 389 (1976)].
2. T. Fukuzawa, E. E. Méndez, and J. M. Hong, Phys. Rev. Lett. **64**, 3066 (1990).
3. J. E. Golub, K. Kash, J. P. Harbison, and L. T. Flórez, Phys. Rev. B **41**, 8564 (1990).
4. J. A. Kash, M. Zachau, E. E. Méndez, *et al.*, Phys. Rev. Lett. **66**, 2247 (1991).
5. L. V. Butov, A. Zrenner, G. A. Abstreĭter, *et al.*, Phys. Rev. Lett. **73**, 304 (1994); L. V. Butov, in *Proceedings of the 23rd International Conference on Physics of Semiconductors, Berlin, 1996*.
6. V. B. Timofeev, A. I. Filin, A. V. Larionov, *et al.*, Europhys. Lett. **41**, 435 (1998).
7. V. B. Timofeev, A. V. Larionov, A. S. Ioselevich, *et al.*, JETP Lett. **67**, 613 (1998).

8. V. V. Krivolapchuk, E. S. Moskalenko, A. L. Zhmodikov, *et al.*, Solid State Commun. **111**, 49 (1999).
9. D. Yoshioka and A. H. MacDonald, J. Phys. Soc. Jpn. **59**, 4211 (1990).
10. X. M. Chen and J. J. Quinn, Phys. Rev. Lett. **67**, 895 (1991).
11. Xuejun Zhu, P. B. Littlewood, M. S. Hybertsen, and T. Rice, Phys. Rev. Lett. **74**, 1633 (1995).
12. J. Fernández-Rossier and C. Tejedor, Phys. Rev. Lett. **78**, 4809 (1997).
13. Lerwen Liu, L. Swierkowski, and D. Nelson, Physica B **249**–**251**, 594 (1998).
14. Yu. E. Lozovik and O. L. Berman, Zh. Éksp. Teor. Fiz. **111**, 1879 (1997) [JETP **84**, 1027 (1997)].
15. V. B. Timofeev, A. V. Larionov, M. Grassi Alessi, *et al.*, Phys. Rev. B **60**, 8897 (1999).
16. *Optical Orientation, Modern Problems in Condensed Matter Sciences*, Ed. by F. Meyer and B. P. Zhakharchenya (Elsevier, Amsterdam, 1984), Vol. 8.

Translated by A. Bagatur'yants

JETP Letters, Vol. 71, No. 3, 2000, pp. 123–126. Translated from Pis'ma v Zhurnal Éksperimental'noĭ i Teoreticheskoĭ Fiziki, Vol. 71, No. 3, 2000, pp. 182–186.

CONDENSED MATTER

Reversal of the Critical-Current Sign in SFIFS Tunnel Contacts

E. A. Koshina and V. N. Krivoruchko[1]

Galkin Donetsk Institute for Physics and Technology, National Academy of Sciences of Ukraine, Donetsk, 83114 Ukraine

Received January 6, 2000

Abstract—The Josephson current is calculated for an SFIFS tunnel contact (where I is an insulator), whose banks are formed by a massive superconductor (S) and a thin layer of a normal ferromagnetic metal (F). Within the microscopic theory of the proximity effect for an SF bilayer, it is shown that, even at mesoscopic dimensions of the ferromagnetic layer in an SFIFS contact, a transition to the state characterized by a π shift of the phase difference between the superconducting wave functions at the banks of the contact can be implemented owing to this effect. The amplitude of the critical current as a function of bilayer parameters is found. It is shown that the exchange-field strength at which the Josephson current in an SFIFS contact is reversed (transition to the π state) can be varied within rather broad limits by changing the parameters of the SF bilayer (resistance of the SF interface and proximity-effect magnitude). © *2000 MAIK "Nauka/Interperiodica".*

PACS numbers: 85.25.Cp; 73.23.Hk; 73.40.-c

1. Among Josephson structures that exhibit in the ground state a spontaneous π shift of the macroscopic phase difference between the superconducting wave functions at the banks of a Josephson junction, SFS junctions seem to show the greatest promise as elements of quantum logic [1, 2]. Although this feature of SF contacts was predicted quite long ago (see [3–5]), the transverse (with respect to the direction of the layers) resistive properties of SFS junctions have been measured only recently (it is worth noting that such measurements are expected to furnish direct information about the transport properties of the systems in question [2, 6, 7]). Moreover, a general theory of tunnel contacts for the case where a normal metal is ferromagnetic has yet to be developed.

The theory of SNINS tunnel junctions (where N and I are, respectively, a normal metal and an insulator) with an arbitrary transparency of SN interface has been considerably developed in recent years (see, for example, [8, 9]). As is well known, a fundamental difference between a nonmagnetic and a ferromagnetic normal metal is that conduction-electron spins are polarized in the latter. In just the same way as in SN structures, the proximity effect in the SF case results in that superconducting correlations are induced in the F layer, but the exchange polarization of electrons near the Fermi surface modifies here the conditions of pairing. In the F layer, there arise two groups (subbands) of electrons: Cooper pairs are formed by quasiparticles from $\{\mathbf{p}\uparrow, (-\mathbf{p} + \Delta\mathbf{p})\downarrow\}$ and $\{\mathbf{p}\downarrow, (-\mathbf{p} - \Delta\mathbf{p})\uparrow\}$ states, where $\Delta\mathbf{p} \sim H_{exc}/v_F$, H_{exc} and v_F are, respectively, the exchange field in energy units and the Fermi velocity. If the spin–orbit scattering of the electrons is sufficiently weak, pairs from the different spin subbands undergo virtually no mixing [10, 11]. Thus, we can conclude that the behavior of SFS junctions is characterized by spatial oscillations [$\cos(\Delta px)$] of the induced superconducting order parameter in the F layer.

Not only does the density of Cooper pairs oscillate in the ferromagnetic layer, but it also decreases exponentially, the characteristic decay length being $\xi_F \sim (D_F/H_{exc})^{1/2}$, where D_F is the diffusion coefficient in the F metal (we use here the system of units in which $\hbar = k_B = 1$). In view of such a strong suppression of superconducting properties by the exchange field, only SF systems where the thickness of the F layer is small, $d_F \ll \xi_F$, and where the exchange field H_{exc} is sufficiently weak are of interest for implementing a π contact in practice. In this limit, however, it is not obvious whether the system in question can occur in a state where the phase difference between the order-parameter values at the banks of the contact is equal to π.

In the present study, the amplitude of the critical current in an SFIFS tunnel contact is analyzed as a function of the parameters of the SF bilayer, such as the proximity-effect magnitude, the transparency of the SF interface, and the exchange-field strength. It is shown that, even at mesoscopic dimensions of the ferromagnetic layer in SFIFS contacts, a state where the phase difference between the order-parameter values at the banks of the contact is equal to π can be realized owing to the proximity effect. An important point is that conditions under which the sign of the Josephson current is reversed can be changed by varying the parameters of the SF bilayer.

[1] E-mail: krivoruc@host.dipt.donetsk.ua

0021-3640/00/7103-0123$20.00

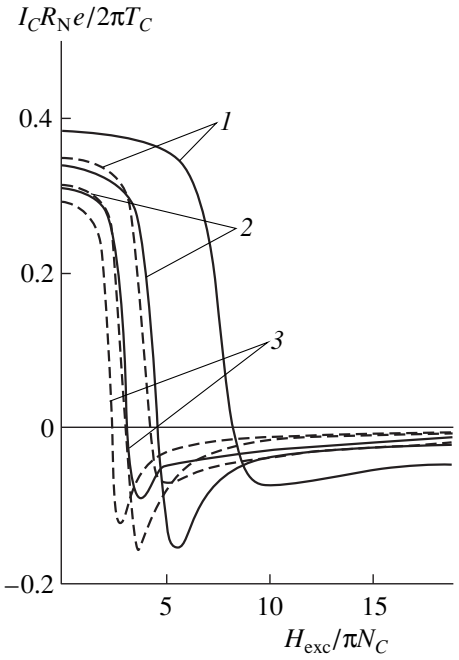

Fig. 1. Critical current of an SFIFS contact for $T/T_C \ll 1$ versus exchange energy at γ_M = (solid curves) 0.1 and (dashed curves) 0.2 for a high transparency of the SF interface: γ_B = (curves *1*) 0, (curves *2*) 0.1, and (curves *3*) 0.2.

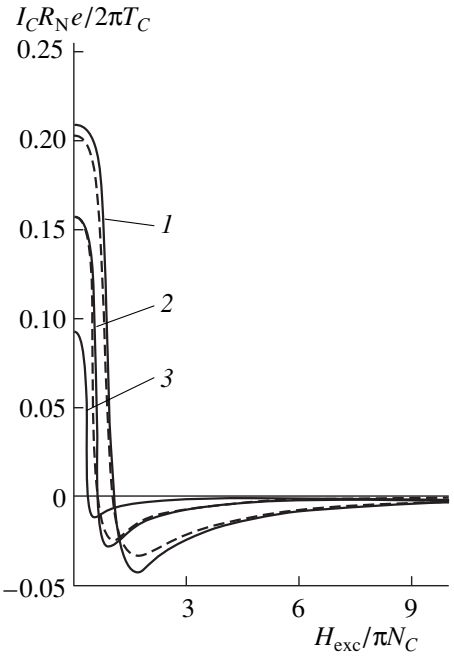

Fig. 2. As in Fig. 1, but for a low transparency of the SF interface: γ_B = (curves *1*) 1, (curves *2*) 2, and (curves *3*) 5. The rest of the notation is identical to that in Fig. 1.

2. Contact model. We will consider the case where either electrode of the tunnel Josephson junction represents an SF bilayer and where the transparency of the insulating layer is so small that the effect of the current on the electrode states can be disregarded. Suppose that the conditions of the dirty limit are satisfied both for the S and for the F metal and that the critical temperature of the superconducting transition in the F metal is zero. We also assume that all the quantities involved depend only on the coordinate along the normal to the interface (the transverse dimensions of the junction are taken to be much less than the Josephson penetration depth λ_J). We will address the most interesting case, that of

$$d_S \gg \xi_S, \quad d_F \ll \min(\xi_F, \xi), \tag{1}$$

where $\xi_S = (D_S/2\pi T_C)^{1/2}$ and $\xi = (D_F/2\pi T_C)^{1/2}$ are the effective coherence lengths in, respectively, the superconducting and the ferromagnetic metal (for the latter, the choice of a convenient coherence length depends on the relationship between the critical temperature T_C of the superconducting metal and H_{exc}), D_S being the diffusion coefficient in the superconducting metal. The first condition in (1) enables us to disregard the reduction of the critical temperature in the SF bilayer in relation to the critical temperature in the bulk S metal. Owing to the second condition, all quantities within the F layer can treated as spatially uniform ones.

The problem of determining the tunnel properties of a junction whose banks are bilayers in close proximity to each other is usually solved in two steps: the superconducting properties of the bilayer involved are determined first, while the electric parameters of the contact are calculated at the next step. For layered systems formed by bulk S layers and thin (mesoscopic) F layers, the proximity effect was considered in [12] without imposing any condition on the transparency of SF interfaces. It was shown there that the interplay of S and F layers is governed by the ratios $\gamma_M = \gamma d_F/\xi$ and $\gamma_B = \gamma_{BF} d_F/\xi$ and by the exchange-field strength H_{exc}. Here, $\gamma = \rho_S \xi_S/\rho_F \xi$ is the proximity-effect parameter characterizing the strength of superconducting correlations induced in the F layer because of the proximity of the S layer; γ_{BF} is a parameter that takes into account effects associated with a finite transparency of the SF interface; and ρ_S and ρ_F are the resistances of, respectively, the S and the F metal in the normal state. (We use here the effective coherence length ξ of the normal nonmagnetic metal with the diffusion coefficient D_F; it is convenient to introduce this quantity for an analysis of the limit $H_{exc} \longrightarrow 0$.) By using general expressions obtained in [12], we will calculate the amplitude of the critical current of an SFIFS contact as a function of parameters of the system such as the proximity-effect magnitude, the transparency of the SF interface, and the strength of the exchange field in the F metal.

3. Critical current of an SFIFS contact. The critical current of the SFIFS tunnel contact can be represented in the form [12]

$$(eR_N/2\pi T_C)I_C = (T/T_C)\mathrm{Re}\Sigma_{\omega>0}G_{F1}(\omega)\Phi_{F1}(\omega)$$
$$\times G_{F2}(\omega)\Phi_{F2}(\omega)/\tilde{\omega}^2 = \mathrm{Re}\Sigma_{\omega>0}\{G_S(\omega)\Phi_S(\omega)/\omega\}^2 \quad (2)$$
$$\times\{1 + 2\omega G_S(\gamma_B/\pi T_C) + \tilde{\omega}^2(\gamma_B/\pi T_C)^2\}^{-1},$$

where R_N is the resistance of the contact in the normal state; $\tilde{\omega} = \omega + iH_{exc}$; $\omega = \pi T(2n + 1)$ ($n = 0, \pm1, \pm2, \ldots$) are Matsubara frequencies; and the subscripts 1 and 2 label quantities referring to the first and the second electrode, respectively. Here, we have taken explicitly into account the normalization condition $G^2 + F^2 = 1$ for the Usadel Green's functions; following [8], we have also introduced the modified Usadel functions $\Phi_{S,F}$ defined by the relations $G_S = \omega/(\omega^2 + \Phi_S^2)^{1/2}$, $F_S = G_S\Phi_S/\omega$, $G_F = \tilde{\omega}/(\tilde{\omega}^2 + \Phi_F^2)^{1/2}$, and $F_F = G_F\Phi_F/\tilde{\omega}$.

Presented below are analytic results obtained by considering the proximity effects for an SF bilayer characterized by a small value of the proximity-effect parameter, $\gamma_M \ll 1$. For the function $\Phi_S(\omega) \equiv \Phi_S(\omega, 0)$, expression (14) from [12] yields

$$\Phi_S(\omega) = \Delta_0\left(1 - \frac{\gamma_M\beta\tilde{\omega}}{\gamma_M\beta\tilde{\omega} + \omega A}\right), \quad (3)$$

where Δ_0 is the absolute value of the order parameter in the bulk of the S layer,

$$\beta = [(\omega^2 + \Delta_0^2)^{1/2}/\pi T_C]^{1/2},$$
$$A \equiv A(\omega) = \left(1 + \frac{\gamma_B\tilde{\omega}}{(\pi T_C)^2}\left(\frac{2\omega}{\beta^2} + \gamma_B\tilde{\omega}\right)\right)^{1/2}.$$

With the aid of (3), expression (2) for the critical current can be reduced to an analytic form that is valid for $\gamma_M \ll 1$ and for an arbitrary transparency γ_B of the SF interface and an arbitrary exchange-field strength. We note that, for $H_{exc} \longrightarrow 0$, $\tilde{\omega} \longrightarrow \omega$ and the value found for I_C goes over to that obtained in [8] for an SNINS contact.

For the case of a weak proximity effect ($\gamma_M \ll 1$), Figs. 1 and 2 show the amplitude of the Josephson current calculated numerically by formulas (2) and (3) versus the exchange-field strength. These results were obtained at a high ($\gamma_B \ll 1$) and a low ($1 \leq \gamma_B$) transparency of the SF interface (Figs. 1 and 2, respectively). It can be seen that, in some interval of exchange-field strengths within the F layer, a state is formed that corresponds to the reversal of the supercurrent; that is, the phase difference between the superconducting order parameters at the different banks of the junction changes by π in this case. A transition to the state where there is a π shift of the phase difference depends greatly on the bilayer parameters γ_M and γ_B. By varying these parameters, we can change sizably the conditions under which the state characterized by a π phase difference at the banks of the junction is realized. To illustrate this statement, we note that, at $\gamma_M = 0.1$, the current is reversed at $H_{exc} \approx 8\pi T_C$ if $\gamma_B = 0.0$ and at $H_{exc} \approx 3\pi T_C$ if $\gamma_B = 0.2$ (see solid curves in Fig. 1). Similarly, the current is reversed at $H_{exc} \approx 3\pi T_C$ rather than at $H_{exc} \approx 8\pi T_C$ if $\gamma_B = 0.1$ but $\gamma_M = 0.2$ (see dashed curves in Fig. 1). In the absence of proximity effects ($\gamma_M = 0$), there is no reversal of the critical current.

The physics behind the phenomenon in question is as follows. Because of proximity effects, ferromagnetic correlations are induced in the S layer over a region that is adjacent to the F layer and which has a thickness of about ξ_S [12]. As a result, the effective thickness of the magnetic layer appears to be on the order of ξ_S. In the case of a sufficiently thick ferromagnetic layer, a transition to the π state becomes energetically favorable (see, for example, [5, 13]).

In the mean-field approximation, within which we treat here ferromagnetism, the exchange field H_{exc} is proportional to the product of the exchange-interaction constant and the magnetization $M(T)$. Since $M(T) \approx M_0[1 - (T/T_0)^{3/2}]$, the exchange-field strength in a given Josephson contact can be changed experimentally by varying the temperature of the contact. Experiments of this type were performed by Veretennikov *et al.* [6] and by Ryazanov *et al.* [7], who found Josephson supercurrents in sandwiches featuring CuNi ferromagnetic layers. In response to a variation in the temperature, the critical current of the junction changed monotonically, undergoing a sign reversal at some point. In all probability, the parameters of the junctions studied in [6, 7] were close to those at which the sign of the critical current is reversed owing to a transition to the π state, and this transition occurred when the varied temperature reached the corresponding value.

ACKNOWLEDGMENTS

We are grateful to A.I. Buzdin for reading the manuscript and for a discussion of it, to A.A. Golubov for enlightening comments on the results presented here. Thanks are also due to V.V. Ryazanov for informing us about the experimental results from [6, 7] prior to their publication and for interest in this study.

REFERENCES

1. M. V. Feĭgel'man, Usp. Fiz. Nauk **169**, 917 (1999).
2. V. V. Ryazanov, Usp. Fiz. Nauk **169**, 920 (1999).
3. A. I. Buzdin, L. N. Bulaevskiĭ, and S. V. Panyukov, Pis'ma Zh. Éksp. Teor. Fiz. **35**, 147 (1982) [JETP Lett. **35**, 178 (1982)].

4. A. I. Buzdin and M. Yu. Kupriyanov, Pis'ma Zh. Éksp. Teor. Fiz. **53**, 308 (1991) [JETP Lett. **53**, 321 (1991)].
5. A. V. Andreev, A. I. Buzdin, and R. M. Osgood, Phys. Rev. B **43**, 10124 (1991).
6. A. V. Veretennikov, V. V. Ryazanov, V. A. Obozov, *et al.*, Physica B (1999).
7. V. V. Ryazanov, V. A. Obozov, A. V. Veretennikov, *et al.*, in *Proceedings of International Seminar "Chernogolovka 99," Quasi-Two-Dimentional Metal and Superconducting Systems, Chernogolovka, Russia, 1999*, p. 46.
8. A. A. Golubov and M. Yu. Kupriyanov, Zh. Éksp. Teor. Fiz. **96**, 1420 (1989) [Sov. Phys. JETP **69**, 805 (1989)].
9. A. A. Golubov, E. P. Houwman, J. G. Gijsbertsen, *et al.*, Phys. Rev. B **51**, 1073 (1995).
10. E. A. Demler, G. B. Arnold, and M. R. Beasley, Phys. Rev. B **55**, 15174 (1997).
11. J. Aarts, J. M. E. Geers, E. Brück, *et al.*, Phys. Rev. B **56**, 2779 (1997).
12. E. A. Koshina and V. N. Krivoruchko, Fiz. Nizk. Temp. **26**, 157 (2000).
13. Z. Radovic, M. Ledvij, and L. Dobrosavljevic-Grujic, Phys. Rev. B **44**, 759 (1991).

Translated by A. Isaakyan

JETP Letters, Vol. 71, No. 3, 2000, pp. 97–101. Translated from Pis'ma v Zhurnal Éksperimental'noĭ i Teoreticheskoĭ Fiziki, Vol. 71, No. 3, 2000, pp. 145–151.

GRAVITY, ASTROPHYSICS

Muons in Extensive Air Showers of Energies $E_0 = 10^{16.6}$–$10^{19.8}$ eV

A. V. Glushkov[1], I. T. Makarov[1], M. I. Pravdin[1], I. E. Sleptsov[1], V. R. Sleptsova[1], and N. N. Kalmykov[2]

[1] *Institute of Cosmophysical Research and Aeronomy, Yakut Research Center, Siberian Division, Russian Academy of Sciences, pr. Lenina 31, Yakutsk, 677891 Russia*

[2] *Skobel'tsyn Research Institute of Nuclear Physics, Moscow State University, Vorob'evy gory, Moscow, 119899 Russia*

Received December 22, 1999

Abstract—Data on muons with the threshold energy $E_\mu \approx 1.0 \times \sec\theta$ GeV in extensive air showers of energies $E_0 \geq 4 \times 10^{16}$ eV measured on the Yakutsk and Akeno arrays are jointly analyzed. The results are compared with the calculations by the quark–gluon–string model with jets. It is shown that this model does not contradict the data measured for energies $E_0 \leq 10^{18}$ eV on both arrays under the assumption that the primary particle composition differs from the composition where heavy nuclei dominate over protons. Experimental data for energies $E_0 \geq 3 \times 10^{18}$ eV indicate that the shower development differs from that predicted by the quark–gluon–string model with jets. © *2000 MAIK "Nauka/Interperiodica".*

PACS numbers: 96.40.Pq; 95.85.Ry; 13.85.Tp

1. INTRODUCTION

Muons of energies ~0.5–1.0 GeV constitute a very important component of the extensive air showers (EASs) induced by cosmic rays of extremely high energies. They are weakly absorbed in the atmosphere and are sensitive to the characteristics of nuclear interactions occurring in the course of EAS development and to the chemical composition of the primary cosmic rays. The number and lateral distribution of muons with the indicated energies allow their detection by the arrays with large distances (~0.5–1.5 km) between detectors. In particular, the basic shower parameters (arrival direction and energy of primary particles) were found by the Sydney group [1] from the data measured on the SUGAR array for the muons with the threshold energy $E_\mu \approx 0.75 \times \sec\theta$ GeV.

The Yakutsk array has been detecting muons with the threshold energy $E_\mu \approx 1 \times \sec\theta$ GeV continuously since 1978. An analysis of a large body of experimental data accumulated during this time period demonstrates [2–9] that the dynamics of EASs with energies $E_0 \geq (3–5) \times 10^{18}$ eV substantially differs from that at lower energies of the primary particles. For a variety of reasons, this conclusion has not yet been confirmed by other researches. In particular, the above-mentioned SUGAR array has long been closed down. Only a few showers of energies $E_0 \geq 10^{18}$ eV, for which muons were detected [10], were observed on the Haverah Park array in England (which is also no longer in operation). The Akeno array in Japan has been detecting muons in EASs with energies of up to ~10^{20} eV for a rather long time [11].

Below, we consider some results obtained for muons on the Yakutsk and Akeno arrays. The experimental data are compared with the results of our calculations carried out in the quark–gluon–string model with jets (QGSJET model) [12] that adequately describes a large body of experimental data on the EASs with energies $E_0 \leq (2–4) \times 10^{18}$ eV [9, 13, 14]. Recent analysis [15] has demonstrated that this model, in a sense, provides the best description in the energy range ~10^6 GeV because it yields identical estimates for the mass composition of cosmic rays when studying different characteristics of EASs in the bend region of the primary energy spectrum.

2. RESULTS AND DISCUSSION

Below, we consider the lateral distribution functions (LDFs) for muons with the threshold energy $E_\mu \approx 1 \times \sec\theta$ GeV. The methods of their determination on both arrays were described in [9, 16]. The Yakutsk LDFs are approximated by the function [9]

$$\rho_\mu(R) = f_\mu(1 + R/2000)^{-6.5} \quad [\mathrm{m}^{-2}] \qquad (1)$$

with the well-known Greisen relationship [17]

$$f_\mu = N_\mu(C_\mu/R_0)r^{-0.75}(1 + r)^{0.75 - b_\mu}, \qquad (2)$$

where $r = R/R_0$ (R_0 = 280 m), C_μ is the normalization constant, N_μ is the total number of muons at the obser-

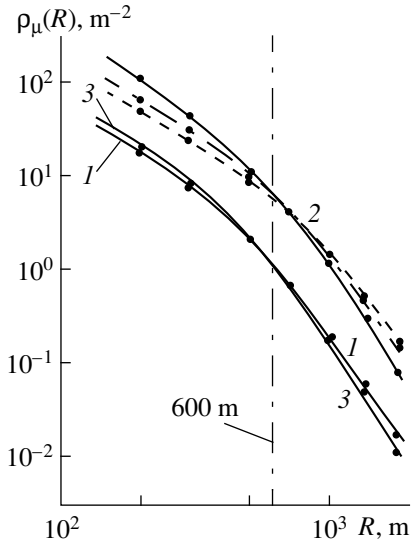

Fig. 1. The LDFs for muons with $E_\mu = 1 \times \sec\theta$ GeV calculated using the QGSJET model for the proton primary composition: the circles are the calculated densities, and the curves are approximation (1) for showers with $E_0 = 3 \times 10^{18}$ eV (*1*, *3*) and 2×10^{19} eV (*2*). Solid, dash–dotted, and dashed lines correspond to $\cos\theta$ = 0.98, 0.78, and 0.58, respectively. Curves *1* and *2* are for the Yakutsk array, and curve *3* is for Akeno.

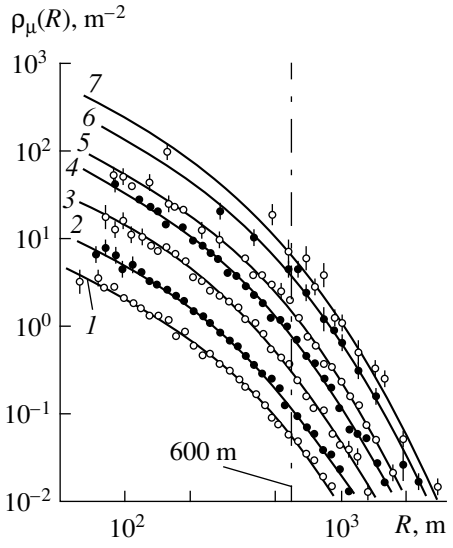

Fig. 2. The LDFs for muons with $E_\mu = 1 \times \sec\theta$ GeV measured on the Yakutsk array in EASs with $\langle\sec\theta\rangle \approx 1.05$: $\log(E_0)$ = 17.1 (*1*), 17.5 (*2*), 17.9 (*3*), 18.3 (*4*), 18.7 (*5*), 19.1 (*6*), and 19.5 (*7*). Curves are approximation (1).

vation level, and b_μ is the parameter depending on the shower energy E_0 and zenith angle θ.

The Akeno data are approximated as [16]

$$\rho_\mu(R) = f_\mu(1 + (R/800)^3)^{-0.6}, \quad (3)$$

where f_μ has the form (2) with $b_\mu = 3.27$ for all showers, while the parameter R_0 depends on the zenith angle θ:

$$\log(R_0) = (0.58 \pm 0.04)(\sec\theta - 1) + (2.39 \pm 0.05). \quad (4)$$

An analysis has shown that expression (1) is well suited also for the description of the Akeno LDFs in the interval 100–3000 m, because functions (1) and (3) are rather close to one another, provided that the parameters b_μ or R_0 are properly chosen. For this reason, to compare the muon LDFs for both arrays, we used only approximation (1), where the b_μ parameters for the Akeno data were found by the least squares method from the experimentally measured densities with allowance made for their errors.

Figure 1 shows the QGSJET-calculated LDFs for the muons induced by primary protons (points) and approximation (1) found from these points for the showers with energies $E_0 = 3 \times 10^{18}$ eV and 2×10^{19} eV (curves). The solid, dash–dotted, and dashed lines correspond to $\cos\theta$ = 0.98, 0.78, and 0.58, respectively. Curves *1* and *2* are for the LDFs in the above-mentioned showers at the Yakutsk observation level, and curve *3* is the same for the Akeno array.

Figures 2 and 3 show the experimental muon LDFs and their fits for the near-vertical-incident EASs observed, respectively, on the Yakutsk and Akeno arrays [16–18]. The LDFs presented in [18] for the muons with threshold energy $E_\mu = 0.5$ GeV are recalculated to $E_\mu = 1.0$ GeV using the Greisen spectrum [19]

$$F(\geq E_\mu, R) = (51/(50 + E_\mu))(3/(2 + E_\mu))^{\varphi(R)}, \quad (5)$$

where $\varphi(R) = 0.14R^{0.37}$. This relationship does not contradict the QGSJET results.

It is seen that approximation (1) satisfactorily fits the experimental data for all distances R from the shower axes (core distances) where measurements were made. The behavior of LDFs as a whole can be judged by the parameter b_μ, which is highly sensitive to the LDF variations. This is seen from Fig. 4, where the b_μ parameters in the showers with $\cos\theta \geq 0.9$ are displayed as functions of E_0. The parameters b_μ calculated in the QGSJET model for the LDFs of muons induced by primary protons are shown for Yakutsk by the solid line and for Akeno by the dashed line. These parameters satisfy expression

$$b_\mu = b_0 + b_1(\log E_0 - 18), \quad (6)$$

where b_0 = 1.96 and 2.18 and b_1 = 0.07 and 0.1 for Yakutsk and Akeno, respectively.

Such a behavior of the b_μ parameter reflects the physical fact that the LDF steepens with a decrease in the $X - X_m$ distance from the observation level X to the level X_m of maximum shower development, because muons concentrate closer to the shower axis as this distance diminishes.

Figure 4 shows the experimental results (crosses) obtained on the Yakutsk array. For energies $E_0 \leq 10^{18}$ eV, they satisfy equation (6) with $b_0 = 2.05 \pm 0.02$ and $b_1 = 0.17 \pm 0.03$. The discrepancy between the calculated and experimental values of the b_1 coefficient characterizing the degree of muon LDF steepening with an increase in E_0 is likely due to an additional change in the composition of primary particles:

$$b_1 \approx 0.07 \times (1 - \partial \log A / \partial \log E_0), \qquad (7)$$

where A is the mass number.

It follows from (7) and measurements that $\partial \log A / \partial \log E_0 \approx -1.43 \pm 0.43$. This, in turn, is not contradictory to the hypothesis that the primary composition changes from a mixture enriched at $E_0 \sim 10^{17}$ eV with heavy nuclei {Z = 10–30 comprise ~(63 ± 7)% [20]} to a lighter mixture. According to estimation [21], the fraction of protons is ~80% ($\langle \ln A \rangle \approx 0.4$) at $E_0 \sim 10^{18}$ eV. On the whole, the Yakutsk data are in agreement with the theoretical results.

For $E_0 \geq (2\text{–}4) \times 10^{18}$ eV, the muon LDF becomes smoother (see Fig. 4) than is expected from the extrapolation of the experimental LDF dynamics from the energy range $E_0 \approx (4\text{–}20) \times 10^{17}$ eV. This anomaly is manifested in the fact that the decrease in the b_μ parameter (by $\Delta b_\mu \approx -0.35$ at $E_0 \sim 10^{19}$ eV) is ~2.7 times greater than the value of $b_\mu(p) - b_\mu(\mathrm{Fe}) = 0.13$ predicted by the QGSJET model for the extreme cases of changing composition from primary protons to iron nuclei. In our opinion, such a behavior of the muon LDF is associated with some new EAS dynamics.

Let us consider the Akeno data. Figure 4 displays the b_μ parameters (triangles and circles) for the LDFs presented in Fig. 3. As seen, the results of different measurement runs are not fully consistent with each other. Moreover, the LDFs obtained on the Akeno array turned out to be considerably smoother than those from the Yakutsk array, although the QGSEJET model predicts the reverse situation. It is conceivable that the data [16–18] contain systematic errors that bring about these discrepancies.

The dash–dotted line in Fig. 4 is the result of recalculation of empirical formula (3) obtained from the Akeno data [16–18] to approximation (1). Our data (crosses in Fig. 4) demonstrate that the muon LDFs may appear to be independent of the energy of primary particles if the experimental accuracy is insufficient. However, this conclusion is erroneous, which becomes clear upon a more detailed and accurate investigation of the muon LDF.

Besides the b_μ parameter, the muon density $\rho_{\mu,\,600}$ measured at a core distance of 600 m is another important parameter determining the magnitude of the muon LDF. One can see from Fig. 1 that at fixed energy E_0 this parameter weakly depends on the zenith angle θ and levels of the Yakutsk and Akeno array locations. It

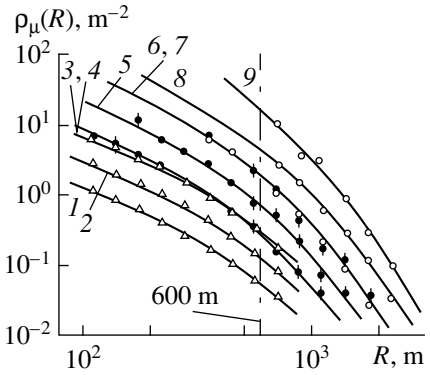

Fig. 3. The LDFs for muons with $E_\mu = 1 \times \sec\theta$ GeV measured on the Akeno array in showers with $\langle \sec\theta \rangle \approx 1.05$: $\log(E_0) = 16.75$ (*1*), 17.25 (*2*), 17.70 (*3*), 17.75 (*4*), 18.25 (*5*), and 18.75 (*6*); and with $\langle \sec\theta \rangle \approx 1.09$: $\log(E_0) = 18.75$ (*7*), 19.25 (*8*), and 19.75 (*9*). Curves are approximation (1). Experimental data are taken from [16] (triangles), [17] (full circles), and [18] (open circles).

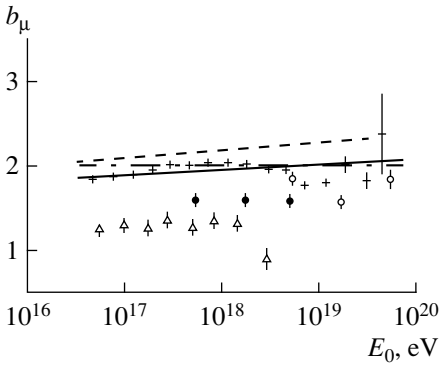

Fig. 4. Plots of parameter b_μ versus energy E_0 in EASs with $\langle \sec\theta \rangle \approx 1.05$ measured on the Yakutsk array (crosses) and the Akeno array (triangles [16], solid circles [17], and open circles [18]); the solid line corresponds to the QGSJET calculation with the proton primary composition for Yakutsk, and the dashed line is the same for Akeno. The dash–dotted line is the recalculation of approximation (3) to (1).

can be experimentally measured over in a wide range of primary particle energies (Figs. 2 and 3) and, for this reason, is often used in quantitative relationships between various EAS characteristics.

Plots of $\rho_{\mu,\,600}$ vs. energy E_0 are shown in Fig. 5 for the showers with $\sec\theta \leq 1.1$. The solid and dashed lines correspond to the QGSJET calculations for Yakutsk and Akeno, respectively. These results satisfy dependence

$$\rho_{\mu,\,600}(0^\circ) = \alpha (E_0/10^{18})^\beta \ [\mathrm{m}^{-2}], \qquad (8)$$

which gives for the primary protons $\alpha(p) = 0.44$ and $\beta(p) = 0.92 \pm 0.01$, for Yakutsk and $\alpha(p) = 0.44$ and $\beta(p) = 0.91 \pm 0.01$ for Akeno.

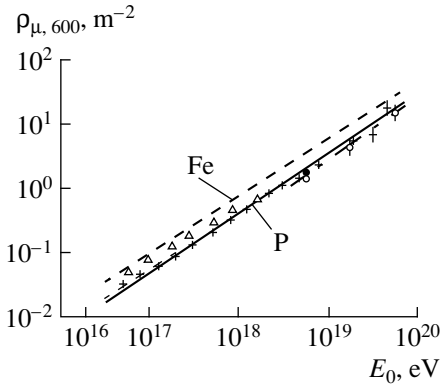

Fig. 5. Plots of $\rho_{\mu,600}$ versus energy E_0 in EASs with $\langle\sec\theta\rangle \approx 1.05$. Notations are as in Fig. 4. The dash–dotted line is the most probable dependence for $E_0 \geq 3 \times 10^{18}$.

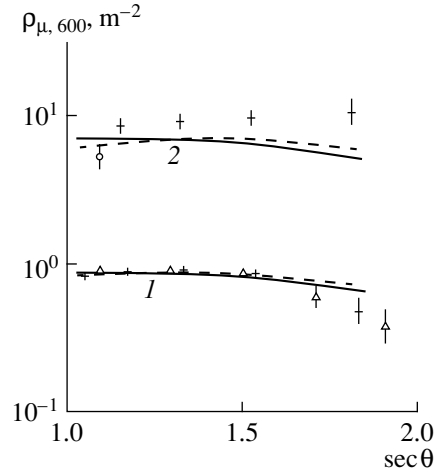

Fig. 6. Plots of $\rho_{\mu,600}$ versus zenith angle in showers with $E_0 = 2 \times 10^{18}$ eV (*1*) and 2×10^{19} eV (*2*). Notations are as in Fig. 4.

The $\rho_{\mu,600}(E_0)$ values obtained on the Yakutsk array are shown in Fig. 5 by crosses. The energy of primary particles was determined as in [2–9]:

$$E_0 = 4.8 \times 10^{17} (\rho_{s,600}(0°))^{1.0} \text{ [eV]}, \quad (9)$$

$$\rho_{s,600}(0°) = \rho_{s,600}(\theta) \exp((\sec\theta - 1) \times 1020/\lambda_p) \text{ [m}^{-2}\text{]}, \quad (10)$$

$$\lambda_p = 450 + 32\log(\rho_{s,600}(0°)) \text{ [g/cm}^2\text{]}, \quad (11)$$

where $\rho_{s,600}(\theta)$ is the charged-particle density measured by ground-based scintillation detectors at a core distance of 600 m. Our data satisfy expression (8) with the following parameters, different in different energy ranges:

$$\alpha = 0.36 \pm 0.02, \ \beta = 0.82 \pm 0.02 \text{ at } E_0 \leq 10^{18} \text{ eV},$$

$$\alpha = 0.32 \pm 0.02, \ \beta = 1.01 \pm 0.04 \text{ at } E_0 \geq 3 \times 10^{18} \text{ eV}.$$

The fact that $\rho_{\mu,600}$ increases more slowly with increasing shower energy in the range $E_0 \leq 10^{18}$ eV confirms the hypothesis that the primary particle composition can change from a mixture enriched with heavy nuclei at $E_0 \sim 10^{17}$ eV to a mixture enriched with protons at $E_0 \sim 10^{18}$ eV. In the first approximation, the superposition model leads to the relationship

$$\beta \approx \beta(p) + (1 - \beta(p))\partial\log A/\partial\log E_0), \quad (12)$$

which, in combination with the Yakutsk data, yields the following estimate for the rate of changing composition: $\partial\log A/\partial\log E_0 = -1.25 \pm 0.37$. This is confirmed by the Akeno data [16], which fit expression (8) with the coefficients

$$\alpha = 0.49 \pm 0.02, \ \beta = 0.80 \pm 0.02 \text{ at } E_0 \leq 3 \times 10^{18} \text{eV}$$

and give an estimate $\partial\log A/\partial\log E_0 = -1.22 \pm 0.22$.

The experimental data presented in Fig. 5 differ from each other in magnitude by a factor of 1.35 at $E_0 \leq 10^{18}$ eV. This contradicts the predictions of calculations and may be caused by various reasons. First, the estimates obtained for E_0 from the $\rho_{s,600}$ values found for the two arrays differ by a factor of 1.15 from each other [22]. Second, the LDFs determined in [16] turned out to be very smooth (Fig. 4). This may be due to the fact that the low muon densities at the shower periphery were overestimated. Third, the Yakutsk data for energies $E_0 \sim 10^{18}$ eV, where the proton primary composition is expected to prevail, are ~1.2 times lower than the results calculated for the proton-initiated EASs. These facts call for further analysis of the details of experimental procedures used on both arrays.

In the energy range $E_0 \geq 3 \times 10^{18}$ eV, the Yakutsk and Akeno data agree with each other within the experimental accuracy but contradict the model under consideration for any composition of primary particles. In this energy range, the most probable $\rho_{\mu,600}(E_0)$ dependence is shown in Fig. 5 by the dash–dotted line with slope $\beta = 1.01 \pm 0.04$.

Figure 6 demonstrates $\rho_{\mu,600}(\theta)$ as a function of the zenith angle for the showers with energies (*1*) $E_0 = 2 \times 10^{18}$ eV and (*2*) 2×10^{19} eV. The crosses are for the experimental data from Yakutsk, and the triangles and circles are for the Akeno data [16, 18]. The solid and dashed lines correspond to the QGSJET calculations (primary protons) for the Yakutsk and Akeno arrays, respectively.

It is seen that the experimental data for $E_0 = 2 \times 10^{18}$ eV agree well both with each other and with the results calculated for $\sec\theta \leq 1.6$. No such agreement was achieved for the EASs with $E_0 = 2 \times 10^{19}$ eV. The Yakutsk data show a more considerable increase in $\rho_{\mu,600}$ with increasing θ than it is predicted by the calculations, while there is as yet no Akeno data on the muon LDFs for inclined showers of such energies.

3. CONCLUSION

The results of the analysis presented in this work can be summarized as follows. The LDFs measured on the Yakutsk and Akeno arrays for muons with threshold energy $E_\mu \approx 1.0 \times \sec\theta$ GeV can be approximated by functions (1) at core distances $R \approx 100$–3000 m. In the energy range $E_0 \leq (1\text{–}2) \times 10^{18}$ eV, the experimental data from both arrays do not contradict the QGSJET model and the assumption that the primary particle composition changes from a mixture dominated by heavy nuclei at $E_0 \sim 10^{17}$ eV {Z = 10–30 comprise ~(63 ± 7)% [20]} to the mainly proton composition at $E_0 \sim 10^{18}$ eV [21]. The discrepancy between the experimental data and calculations is likely associated with the details of measuring the muon LDFs on the arrays considered. Refinement of the QGSJET model is also not improbable.

A different situation takes place at $E_0 \geq 3 \times 10^{18}$ eV. The Yakutsk data (Figs. 4–6) indicate that the shower dynamics in this energy range is different from that predicted by the QGSJET model for any primary particle composition. This conclusion is also confirmed by the anomalously shaped LDFs measured for all charged particles by the ground-based scintillation detectors of the Yakutsk array [9, 23, 24].

Until now, the modern Akeno Giant Air Shower Array (AGASA) covering an area of ~100 km^2 [25] has detected only a few events involving muons in most powerful, primarily inclined, EASs, so that one cannot confidently judge the behavior of LDF in the range $E_0 \geq 5 \times 10^{18}$ eV. Further extension of the shower statistic may not clarify the problem of irregular EAS dynamics in the energy range indicated above, because muon detectors (Geiger–Müller counters of area 0.2 or 0.5 m^2 [25]) used in AGASA have a narrow dynamic range and are saturated at $\rho_\mu \geq 10$–15 m^2. They provide information on the muon distribution at core distances $R \geq 600$–800 m, but this is little for the relative changes in the overall LDF shape to be detected.

ACKNOWLEDGMENTS

This work was supported by the Ministry of Sciences of Russian Federation (support for the Yakutsk complex EAS array included under no. 01-30 into the "Register of the Unique Research and Experimental Instruments of National Significance") and by the Russian Foundation for Basic Research, project no. 98-02-16964. N.N. Kalmykov acknowledges the support of the Russian Foundation for Basic Research, project nos. 96-15-96783 and 99-02-16250.

REFERENCES

1. C. J. Bell, A. D. Bray, S. A. David, *et al.*, J. Phys. A **7**, 990 (1974).
2. A. V. Glushkov, I. T. Makarov, E. S. Nikiforova, *et al.*, Yad. Fiz. **58**, 1265 (1995) [Phys. At. Nucl. **58**, 1186 (1995)].
3. A. V. Glushkov, I. T. Makarov, E. S. Nikiforova, *et al.*, Astropart. Phys. **4**, 1274 (1995).
4. A. V. Glushkov, V. B. Kosarev, I. T. Makarov, *et al.*, Pis'ma Zh. Éksp. Teor. Fiz. **67**, 361 (1998) [JETP Lett. **67**, 383 (1998)].
5. A. V. Glushkov, V. B. Kosarev, I. T. Makarov, *et al.*, JETP Lett. **67**, 383 (1998).
6. A. V. Glushkov, I. T. Makarov, M. I. Pravdin, *et al.*, Izv. Ross. Akad. Nauk, Ser. Fiz. **63**, 538 (1999).
7. A. V. Glushkov, M. I. Pravdin, V. R. Sleptsova, *et al.*, in *Proceedings of 26th International Cosmic Ray Conference, 1999*, Vol. 1, p. 387.
8. A. V. Glushkov, M. I. Pravdin, V. R. Sleptsova, *et al.*, in *Proceedings of 26th International Cosmic Ray Conference, 1999*, Vol. 1, p. 399.
9. A. V. Glushkov, N. N. Kalmykov, M. I. Pravdin, *et al.*, Yad. Fiz. (2000) [Phys. At. Nucl. (2000)] (in press).
10. P. R. Blake and W. F. Nash, J. Phys. G **21**, 129 (1995).
11. Summary of Akeno Experiments. Akeno Observatory, Institute for Cosmic Ray Research, University of Tokyo, 1997.
12. N. N. Kalmykov *et al.*, in *Proceedings of 24th International Cosmic Ray Conference, 1995*, Vol. 1, p. 123.
13. N. N. Kalmykov, S. S. Ostapenko, and A. I. Pavlov, Nucl. Phys. B (Proc. Suppl.) **52**, 17 (1997).
14. M. Nagano, D. Heck, K. Shinozaki, *et al.*, Preprint FZKA No. 6191 (Forschungszentrum Karlsruhe, Karlsruhe, 1998).
15. A. D. Erlykin and A. W. Wolfendale, in *Proceedings of 16th ECRS, Alcalá de Henares, 1998*, p. 269.
16. N. Hayashida, K. Honda, M. Honda, *et al.*, J. Phys. G **21**, 1101 (1995).
17. M. Teshima, Y. Matsubara, T. Hara, *et al.*, J. Phys. G **12**, 1097 (1986).
18. N. Inoue *et al.*, in *Proceedings of 26th International Cosmic Ray Conference, 1999*, Vol. 1, p. 357.
19. K. Greĭsen, Phys. Rev. Lett. **16**, 748 (1966).
20. E. A. Vishnevskaya, N. N. Kalmykov, G. V. Kulikov, *et al.*, Yad. Fiz. **62**, 300 (1999) [Phys. At. Nucl. **62**, 265 (1999)].
21. A. V. Glushkov, L. G. Dedenko, N. N. Efimov, *et al.*, Izv. Akad. Nauk SSSR, Ser. Fiz. **50**, 2166 (1986).
22. M. Nagano, M. Teshima, Y. Matsubara, *et al.*, J. Phys. G **18**, 423 (1992).
23. A. V. Glushkov, M. I. Pravdin, and I. E. Sleptsov, Izv. Ross. Akad. Nauk, Ser. Fiz. **61**, 516 (1997).
24. A. V. Glushkov, M. I. Pravdin, and I. Ye. Sleptsov, in *Proceedings of the 25th International Cosmic Ray Conference, 1997*, Vol. 6, p. 233.
25. N. Chiba, K. Hashimoto, N. Hayashida, *et al.*, Nucl. Instrum. Methods Phys. Res. A **311**, 338 (1992).

Translated by R. Tyapaev